$4f$-$5d$ transitions of Pr^{3+} in elpasolite lattices

P. A. Tanner and C. S. K. Mak
Department of Biology and Chemistry, City University of Hong Kong, Tat Chee Avenue, Kowloon. Hong Kong S. A. R., China

M. D. Faucher
UMR 8580 du CNRS, "Structures, Propriétés et Modélisation des Solides," Ecole Centrale Paris, 92295 Châtenay-Malabry Cedex, France

W. M. Kwok and D. L. Phillips
Department of Chemistry, The University of Hong Kong, Pokfulam Road, Hong Kong S. A. R., China

V. Mikhailik
Physics Department, Lviv State Franko University, Kyryla i Mefodiya Str. 8, 290005 Lviv, Ukraine
(Received 20 May 2002; revised manuscript received 14 November 2002; published 5 March 2003)

The $4f5d \rightarrow 4f^2$ emission spectra of Cs_2MPrCl_6 (M=Na,Li) and $Cs_2NaYCl_6:Pr^{3+}$ have been recorded at temperatures down to 10 K. The spectra of Pr^{3+} in the cubic host Cs_2NaYCl_6 are the most clearly resolved, and 15 transitions to terminal crystal field levels of symmetry representations Γ_{5g} and Γ_{4g} have been observed and assigned, thereby inferring that the symmetry representation of the lowest $4f5d$ crystal field level is Γ_{3u}. Each transition is characterized by strong progressions in two totally symmetric vibrational modes. The relative displacement of the potential energy curves for the $4f^2$ and $4f5d$ crystal field levels, along the α_{1g} internal mode coordinate, is small, being only about 5 pm. The 10-K ultraviolet absorption spectra of $Cs_2NaYCl_6:Pr^{3+}$ are assigned to transitions from the $[^3H_4]$ Γ_{1g} electronic ground state to terminal Γ_{4u} crystal field levels of $4f5d$. Nontotally symmetric gerade vibrational modes only provide minor intensity contributions. The large energy gap between the *d-f* emission and *f-d* absorption spectra of Pr^{3+} in the cubic elpasolite host is rationalized. The 8-K excitation spectra of $Cs_2NaPrCl_6$ and $Cs_2NaYCl_6:Pr^{3+}$, excited by synchrotron radiation, show that the transitions to $4f5d$ fall into two groups. The energy levels and wave vectors of the (independent) $4f^2$ and $4f5d$ configurations of Pr^{3+} have been calculated using a model which includes spin-orbit coupling and crystal field and Coulomb interactions, as well as the configuration interaction of $4f^2$ with $4f6p$. Using the eigenvector of the predominantly high-spin, lowest excited crystal field level of $4f5d$, the emission intensities are reasonably well simulated. However, the refinement of the $4f^2 \rightarrow 4f5d$ absorption intensities requires a more detailed knowledge of the crystal field energy level scheme of $4f5d$. The configuration interaction of $4f5d$ with $4f6s$ and $4f5g$ is discussed.

DOI: 10.1103/PhysRevB.67.115102 PACS number(s): 78.40.−q, 78.20.Bh, 71.55.−i, 71.70.Ch

I. INTRODUCTION

The $4f^N$-$4f^N$ intraconfigurational one-photon transitions of tripositive lanthanide ions, Ln^{3+}, in centrosymmetric environments consist of many complex series of weak bands.[1,2] The zero-phonon lines are enabled by the magnetic dipole[3] and/or electric quadrupole[4] mechanisms, whereas the broader vibronic structure is electric dipole allowed.[5] The interpretation of the one-photon electronic spectra has enabled the comparison of $4f^N$ energy level structures of the lanthanide ions with parametrizations using crystal field theory,[6] further refined by inclusion of the correlated crystal field[7] or configuration interaction.[8] Additional data for the lower electronic states have been forthcoming from inelastic scattering of neutrons[9] and electronic Raman spectroscopy.[10] In general, the overlapping electronic transitions in the region above 20 000 cm^{-1} of the one-photon electronic spectra cannot generally be reliably interpreted. This problem has been surmounted in some suitable cases via the extensive use of two-photon spectroscopy in the assignment of the higher $4f^N$ energy levels.[11]

By contrast to the wealth of reports concerning the $4f^N$-$4f^N$ electronic transitions, there have been fewer studies of the electric-dipole allowed $4f^N$-$4f^{N-1}5d^1$ transitions of Ln^{3+} at centrosymmetric sites in crystals. This is unfortunate because the accurate locations of the $4f^{N-1}5d^1$ energy levels are essential in many detailed calculations, such as of the vibronic intensity in electronic spectra and of the electronic Raman scattering intensities.

Loh extensively investigated the absorption spectra of $CaF_2:Pr^{3+}$ in the ultraviolet region[12,13] and assigned interconfigurational transitions between 44 000 and 69 000 cm^{-1} ($4f^2 \rightarrow 4f^15d^1$) and near 76 000 cm^{-1} ($4f^2 \rightarrow 4f^16s^1$). One of several complications in this system is the overlap of the $4f^2$ and $4f5d$ configurations, and Loh identified[14] the highest term manifold $^1S_0$ of the former at 47 200 cm^{-1} in $CaF_2:Pr^{3+}$. This assignment was subsequently disputed.[15] Although it is clear that the $^1S_0$ level is at 46 986 cm^{-1} in $LaF_3:Pr^{3+}$,[15] the location in $CaF_2:Pr^{3+}$ and $LaCl_3:Pr^{3+}$ appears to be uncertain from one-photon spectra, although two-photon studies have enabled its assignment at 46 451 cm^{-1} in the latter system.[16] The $4f^2 \rightarrow 4f^15d^1$ transitions occur at notably lower energy in $Y_3Al_5O_{12}:Pr^{3+}$, and Gayen and coworkers have investigated how the effects of excited-state

absorption inhibit the laser action based upon the $4f^15d^1 \rightarrow 4f^2$ emission.[17–19]

Theoretical developments,[20] the requirements for vacuum ultraviolet phosphors, coupled with improvements in the construction of vacuum ultraviolet spectrometers[21] and the easier access to synchrotron radiation have led to a recent upsurge of interest in $4f^N$-$4f^{N-1}5d^1$ spectra of rare earths. Just as in the case of $4f^N$-$4f^N$ spectra,[8] the $4f^N$-$4f^{N-1}5d^1$ spectra of lanthanide ions in octahedral symmetry environments comprise much more detailed structure than in the case of low-symmetry systems. Indeed, this was one of our major motivations for the present investigation. Schwartz and Schatz[22] have reported the only high-resolution absorption and magnetic circular dichroism spectral study of octahedral (O_h) Ce^{3+}, at 6 K. Two electronic transitions were observed in the region between 28 150 and 31 000 cm^{-1}, with overlapping progressions in the totally symmetric (ν_s) Ce-Cl stretching mode, $\nu_1\alpha_{1g}$, and another mode of 45 cm^{-1}, assigned to a totally symmetric localized or pseudolocalized lattice mode. The $4f^1 \rightarrow 5d^1$ transitions were assigned, in order of increasing energy, to $[^2F_{5/2}]\Gamma_{7u} \rightarrow \Gamma_{8g}[^2T_{2g}]$ and $[^2F_{5/2}]\Gamma_{7u} \rightarrow \Gamma_{7g}[^2T_{2g}]$. The transition to the $5d^1[^2E_g]$ state was not detected up to 50 000 cm^{-1}, so that $\Delta = 10Dq \geqslant 20\,000\ cm^{-1}$. van't Spijker *et al.*[23] did not comment upon these results in their more recent study of Ce^{3+}-doped elpasolites using room-temperature x-ray excitation, where two bands at 48 780 and 46 512 cm^{-1} were assigned to absorption to the $5d^1[^2E_g]$ state. Since the state ^2E_g transforms as a Kramer's quartet Γ_{8g}, in O_h symmetry, the lower-energy band presumably corresponds to the unresolved hot electronic transitions $[^2F_{7/2}]\Gamma_{7u}$, $\Gamma_{8u} \rightarrow \Gamma_{8g}[^2E_g]$. A further strong band is evident between 52 700 and 55 000 cm^{-1} in the excitation spectra of Ce^{3+} emission.[23] This broad feature could correspond to a ligand to metal charge-transfer transition; and/or to the $4f^1 \rightarrow 6s^1$ transition; and/or to the $4f^N \rightarrow 4f^{N-1}5d^1$ transitions of another lanthanide ion present as an impurity species. Recently, Laroche *et al.*[24] have obtained the $4f^{N-1}5d^1 \rightarrow 4f^N$ emission spectra of $Cs_2NaYCl_6:Ce^{3+}$ and Pr^{3+} by pumping the $^3H_4 \rightarrow {}^3P_0$ f^2-electronic absorption bands of Pr^{3+}. These authors suggested that the corresponding ions doped into Cs_2NaYF_6 might exhibit properties useful for tunable ultraviolet laser operation. In fact, the low-resolution ultraviolet emission and absorption spectra of Ce^{3+} doped into several hexafluoroelpasolite lattices have previously been reported by Aull and Jenssen.[25] In general, the spectra were structureless, and two emitting centres were found, due to intergrowth of a second phase or to disorder. Careful crystal growth of $Cs_2NaYF_6:Ce^{3+}$ and $Cs_2NaYF_6:Pr^{3+}$ enabled their properties as x-ray storage phosphors to be evaluated, but the emission spectra were broad and structureless.[26]

A complication in the investigation of *f-d* absorption transitions is the expected presence of charge-transfer transitions in the (vacuum) ultraviolet region. In the spectra of $CaF_2:Pr^{3+}$, Loh[12,13] assigned the $F^-(2p) \rightarrow Pr^{3+}(6s)$ charge transfer band near 80 000 cm^{-1}. The $F^-(2p) \rightarrow Pr^{3+}(4f)$ and $Cl^-(3p) \rightarrow Pr^{3+}(4f)$ charge-transfer transitions have been assigned in the regions 113 000–121 000 and 72 600–80 700 cm^{-1}, respectively.[27] The lowest-energy charge-transfer bands for some other lanthanide hexahalide complexes have been measured at room temperature in solution.[28] Blasse[29] has noted that the charge-transfer band, whose position is relatively insensitive to the host lattice in Ln^{4+}-doped six-coordinated ternary oxides, shifts to lower energy with increasing lanthanide oxidation state, whereas the $4f^N \rightarrow 4f^{N-1}5d^1$ transition shifts to higher energy. Luminescence from the charge-transfer state has not been observed for Ln^{3+}, except for Yb^{3+}.[30] Whether luminescence is observed from the $4f^2$ $^1S_0$ level or from the lowest $4f^15d^1$ level in Pr^{3+} depends upon the relative locations of these states. For $LaF_3:Pr^{3+}$ (Ref. 15) and $YF_3:Pr^{3+}$ (Ref. 31), the $^1S_0$ level is at the lower energy and luminescence occurs to a ladder of lower states.

The present study represents the first investigation of the $4f^{N-1}5d^1 \leftrightarrow 4f^N$ emission, excitation, and absorption spectra of a lanthanide ion at an octahedral symmetry site. The spectra are considerably more detailed and well resolved than any previously reported for these transitions of Pr^{3+},[32,33] and are presented in Sec. III, after a brief review of experimental details (Sec. II). A preliminary report has been made of some results from the emission spectrum of $Cs_2NaYCl_6:Pr^{3+}$.[34] A theoretical model (Sec. IV) has been developed to simulate the $4f^15d^1$-electron energy levels and the spectral intensities of Pr^{3+} in the present systems. Due to the site symmetry of Pr^{3+}, $4f^N$ and $4f^{N-1}5d^1$ configurations are entirely separate and do not interact in the present case. The conclusions from theory and experiment are made in Sec. V.

II. EXPERIMENT

Polycrystalline samples of $Cs_2NaPrCl_6$ and $Cs_2NaYCl_6:Pr^{3+}$ were prepared in sealed silica tubes by passing dried powders from Morss method E (Ref. 35) through a Bridgman furnace at 850 °C. The Pr_6O_{11} and Y_2O_3 starting materials were of 99.9/99.999% (Strem Chemicals; or Berkshire Ores) and 99.999% (Berkshire Ores) purity, respectively. Crystals were mounted in a homebuilt liquid-nitrogen cryostat or an Oxford Instruments closed-cycle cryostat. Ultraviolet absorption spectra (500–200 nm) were recorded at City University at 10 K using a Perkin-Elmer Lambda-18 Spectrophotometer, with resolution of 1 nm. Single-beam absorption spectra were also recorded using a D_2 lamp and a 0.5-m Acton monochromator with a SpectruMM charge coupled device (CCD) detector system. Xenon-lamp excitation and emission spectra between 200 and 800 nm were recorded at 300 and 80 K, at resolution 2 nm, using a SLM Spectrofluorometer, also at City University. The sensitivity of this instrument decreases markedly, to high energy of 250 nm. Emission and electronic Raman spectra were recorded at 10 K at higher resolution (ca. 0.05 nm, 4 cm^{-1}) at Hong Kong University, from 190 to 800 nm. In these experiments the sample was excited by the H_2-shifted harmonics of a Nd-YAG pulsed laser. The emission was collected at 90° and passed through an Acton 0.5-m spectrometer, with a liquid-N_2-cooled SDS 9000 CCD (Photometrics). All spectra were corrected to vacuum wave numbers. Emission and excitation spectra were also recorded at 8 K be-

tween 50 and 500 nm using vacuum ultraviolet (VUV) synchrotron radiation at HASYLAB, Hamburg, Germany. The full width at half maximum (FWHM) of the exit slit of the primary monochromator was 0.18 nm, and the FWHM of the entrance and exit slits of the secondary monochromator were 0.6 nm.

III. EXPERIMENTAL RESULTS

A. Survey spectra

In the range of our experiments, from 300 to 8 K, the space group symmetry of Cs_2NaYCl_6 remains cubic, $Fm3m$-O_h^5, but that of $Cs_2NaPrCl_6$ changes from O_h^5 at room temperature to C_{4h}^5 at 156 ± 3 K.[36,37] The symmetry descent leads to splittings of degenerate $4f^2$-electron levels by up to ca. 20 cm^{-1}.[2]

The Lambda-18 low-resolution 10-K absorption spectra (not included herein) of $Cs_2NaPrCl_6$ and $Cs_2NaY_{0.98}Pr_{0.02}Cl_6$ between 500 and 200 nm (20 000–50 000 cm^{-1}) show weak bands extending up to 440 nm (22 700 cm^{-1}) due to intraconfigurational $4f^2$-$4f^2$ transitions.[8] To higher energy a feature is observed at ca. 340 nm (29 400 cm^{-1}) which sharpens into ten bands at 8 K and is identified as $4f^1\rightarrow5d^1$ absorption of Ce^{3+} impurity,[22] due to its intensity behavior in the 99.9% Pr and 99.999% Pr purity samples. Between 252 and 262 nm (39 680–38 170 cm^{-1}) a sharp rise in absorption is observed, marking the onset of $4f^2\rightarrow4f^15d^1$ absorption of Pr^{3+}. The strong absorption continues to 200 nm, and our absorption intensity measurements are not reliable at energies above the onset.

The survey 80-K emission spectrum of $Cs_2NaPrCl_6$ under 260-nm Xe-lamp excitation is shown in Fig. 1(a), and the band energies, including those not shown at lower energy, are listed in Table I. Although the Pr^{3+} emission spectrum in $Cs_2NaPrCl_6$ consists of relatively broad, unresolved features, it is possible to identify the terminal *SLJ* term manifolds of the Pr^{3+} $4f^2$ configuration from the band spacing intervals (Table I), so that it is clear that the transitions correspond to $4f^15d^1\rightarrow4f^2$. The spectrum contains a similar information content to the reported $LiYF_4:Pr^{3+}$ emission spectrum at 10 K.[32] Figure 1(a) is similar to the 487-nm excited 77-K spectrum of Pr^{3+} reported by Laroche *et al.*,[24] where the excited configuration is populated by upconversion, except that the $4f^15d^1\rightarrow4f^2[^3H_4]$ transition is observed in the latter spectrum as a broad feature at 263 nm. As evident in other studies,[24,38] two Ce^{3+} $5d^1\rightarrow4f^1$ emission bands are observed in Fig. 1(a) near 368 and 404 nm. Since the excitation energy does not match that of Ce^{3+} absorption bands, the energy-transfer process

$$\begin{aligned} &Pr^{3+}\ \ 4f^15d^1(\text{site}\ \ 1)+Ce^{3+}[^2F_{5/2}]4f^1(\text{site}\ \ 2)\\ &\quad\rightarrow Pr^{3+}[^1G_4]4f^2(\text{site}\ \ 1)+Ce^{3+}[^2D_{5/2}]5d^1(\text{site}\ \ 2)\\ &\qquad+n\ \ \text{phonons}, \end{aligned} \tag{1}$$

where $n\geqslant2$, is responsible for populating the luminescent $Ce^{3+}[^2D_{5/2}]\Gamma_8$ state. These Ce^{3+} emission bands, due to trace impurities, are absent in the corresponding emission spectrum of $Cs_2NaY_{0.98}Pr_{0.02}Cl_6$ and are not subsequently referred to. Band 6 in Fig. 1(a) corresponds to the intraconfigurational $^3P_0\rightarrow{}^3H_4$ transition of Pr^{3+}.[2] No emission is observed from the $4f^2[^1S_0]$ level, which is calculated to be near 45 000 cm^{-1},[8] and therefore decays by intersystem crossing to the $4f^15d^1$ levels.

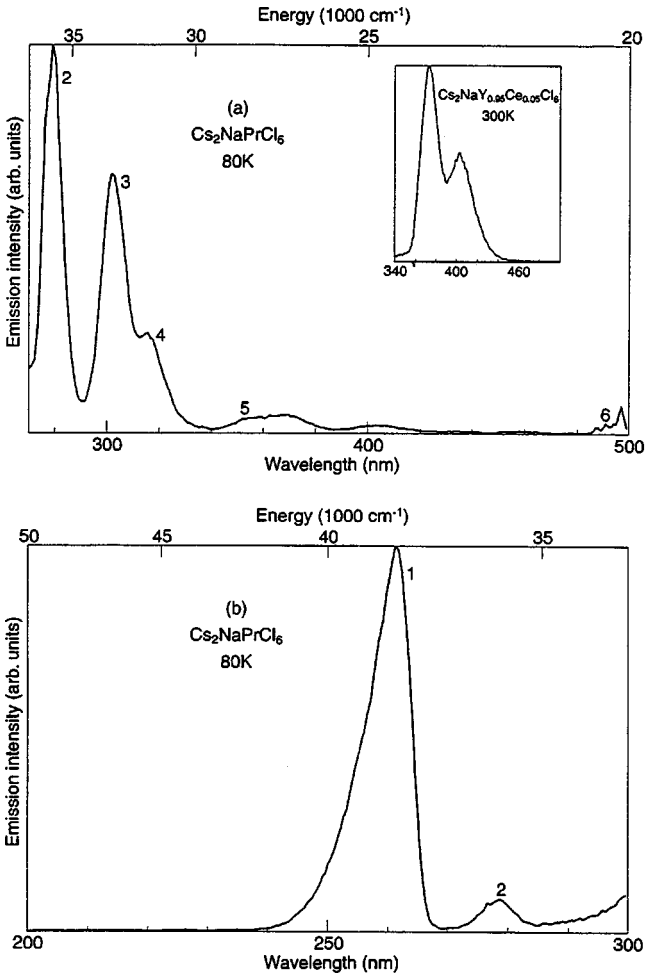

FIG. 1. 261-nm Xe-lamp excited 80-K emission spectrum (a) and 302-nm excitation spectrum (b) of $Cs_2NaPrCl_6$. The inset in (a) shows the 300-K emission spectrum of $Cs_2NaYCl_6:Ce^{3+}$. Refer to Table I for band energies. The spectra are uncorrected for instrumental response, which falls off to high energy.

TABLE I. Assignment of bands in the 260-nm excited 80-K emission spectrum (Fig. 1) and 252.7-nm excited 10-K emission spectrum (Fig. 3) of $Cs_2NaPrCl_6$.

Line, Figs. 1(a), 1(b)	Energy maximum (cm^{-1})	Energy difference (cm^{-1}) from band 1	Line, Figs. 3(a)–3(c)	Assignment of terminal $4f^2$ term manifold
1	38300		1–7	$^3H_4$
2	35970	2330	8–14	$^3H_5$
3	33100	5200	15–22	$^3H_6$, $^3F_2$
4	31750	6550	23–26	$^3F_3$, $^3F_4$
5	28490	9810	27–35	$^1G_4$
	21650	16650		$^1D_2$

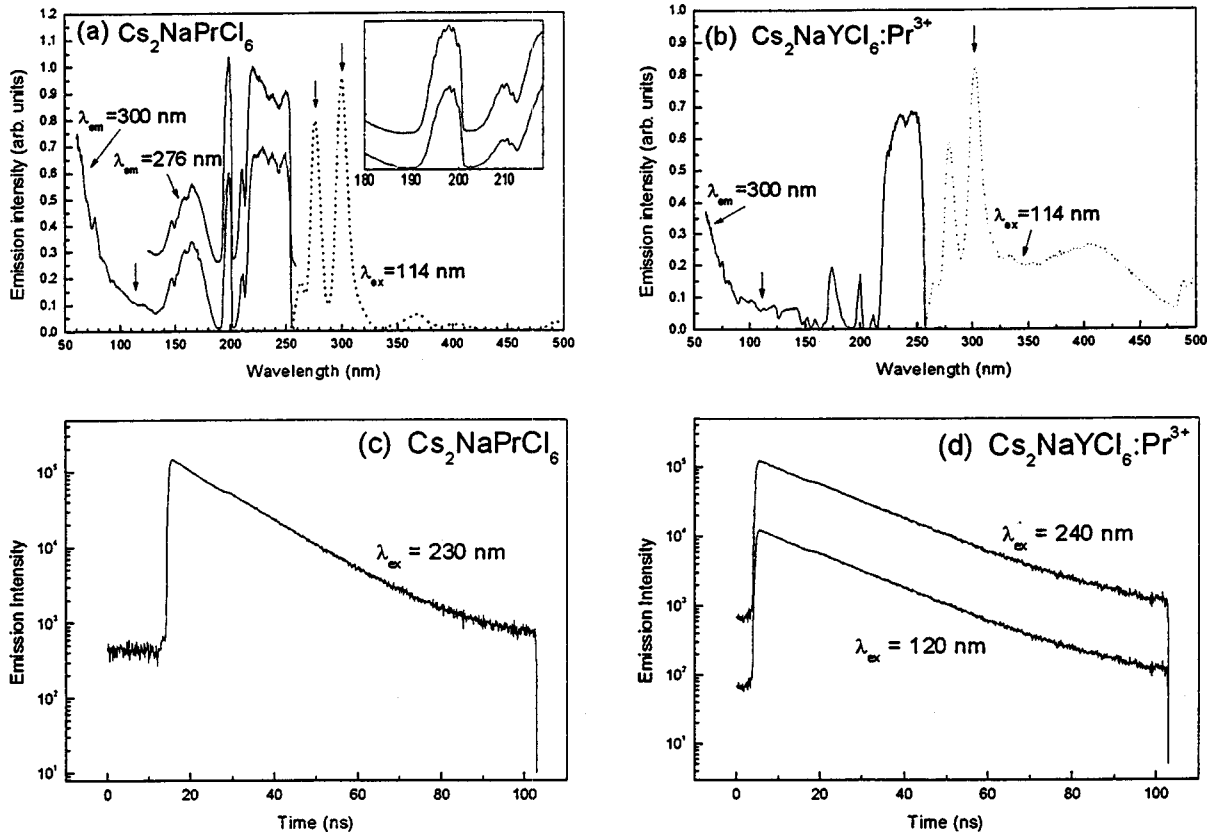

FIG. 2. Synchrotron radiation excited emission (dotted lines) and excitation spectra (solid lines) of (a) $Cs_2NaPrCl_6$ and (b) $Cs_2NaY_{0.99}Pr_{0.01}Cl_6$ at 8 K. The inset in (a) shows the region between 47 000 and 51 000 cm^{-1} in more detail. (c) 8-K decay of $4f^15d^1 \rightarrow 4f^2$ emission near 300 nm for $Cs_2NaPrCl_6$ and (d) $Cs_2NaY_{0.99}Pr_{0.01}Cl_6$. The kink in the profiles is an artifact due to the photomultiplier autopulse.

Figure 1(b) shows the 80-K excitation spectrum of the 302-nm (33 100-cm^{-1}) emission band of $Cs_2NaPrCl_6$. The spectrum is similar to the excitation spectra of the other $4f^15d^1 \rightarrow 4f^2$ emission bands and to that of the $4f^2[^3P_0]$ emission. Band 2 in Fig. 1(b), at 278–282 nm (35 970–35 460 cm^{-1}), is variable from sample to sample, and coincides not only with the hot electronic transitions of Pr^{3+}, from the $^3H_5$ term to $4f^15d^1$, but also with the Ce^{3+} $4f^1 \rightarrow 5d^1$ absorption band. Band 1, Fig. 1(b), cuts off at about 240 nm, due to the decrease in instrumental sensitivity. The latter assertion is confirmed by the synchrotron excitation spectra of the emission at 276 and 300 nm, Figs. 2(a) and 2(b), where the intense $4f^2 \rightarrow 4f^15d^1$ absorption band extends up to 220 nm (45 500 cm^{-1}). Since the f^2 ground state is $[^3H_4]\Gamma_{1g}$, then transitions are electric dipole allowed to each of the 18 Γ_{4u} crystal field levels of $4f^15d^1$. In each case, the same vibrational progression modes as those observed in emission are expected to be active. However, it is not straightforward to identify the terminal states since the spectral resolution is inadequate and, furthermore, extensive overlap of transitions occurs, with each one extending over 1000 cm^{-1}. The $4f^2 \rightarrow 4f^15d^1$ transitions exhibit total absorption in (a) between 252.9 nm (39 540 cm^{-1}) and 216.5 nm (46 180 cm^{-1}).

Loh[12–14] assigned three sets of bands between 45 000 and 70 000 cm^{-1} in the absorption spectra of $CaF_2:Pr^{3+}$ to $4f^2 \rightarrow 4f^15d^1$ absorption transitions of isolated and cluster Pr^{3+} ions, with weak bands near 76 000 cm^{-1} being associated with $4f^2 \rightarrow 4f^16s^1$ transitions. Brewer[39] subsequently placed $4f^16s^1$ above 100 000 cm^{-1}. However, Elias *et al.* assigned the $4f^2 \rightarrow 4f^16s^1$ transitions at 80 000 cm^{-1} in $LaF_3:Pr^{3+}$,[40] whereas Reid *et al.*[33] assigned three groups of bands between 46 000 and 70 000 cm^{-1} in the excitation spectrum of $LiYF_4:Pr^{3+}$ to $4f^2 \rightarrow 4f^15d^1$ transitions. In the present study, the sharper, weaker features near 200 and 210 nm could be assigned to the $4f^2 \rightarrow 4f^16s^1$ transitions, but the corresponding bands are then some 30 000 cm^{-1} to lower energy than those assigned in $LaF_3:Pr^{3+}$.[40] These weaker, sharper bands are not due to Nd^{3+} impurity. Wybourne[41] has described the states of $4f^16s^1$ using the J_1jJ coupling scheme, where J_1 represents the $J=7/2,5/2$ core states of $4f^1$, and j is the s-electron angular momentum. Two groups of states are therefore expected for the $4f^16s^1$ configuration, with a separation similar to that between the $^2F_{5/2}$-$^2F_{7/2}$ terms of Ce^{3+} (i.e., 2000–3000 cm^{-1}). Our preliminary calculations show that the separation of the two $4f6s$ triplet states $[^3F_3]\Gamma_{4u}$ and $[^3F_4]\Gamma_{4u}$ is about 2600 cm^{-1}, and although transitions to these levels from the $4f^2[^3H_4]\Gamma_{1g}$ level are electric dipole forbidden, they become allowed if

the $4f6s$ configuration is mixed with $4f5d$. The inset in Fig. 2(a) shows the spectral region in $Cs_2NaPrCl_6$ near 200 nm in greater detail. Two electronic origins can be assigned at 47 211 and 49 922 cm^{-1}, with this expected separation. A progression in a vibrational mode of 276 cm^{-1} is based upon each zero-phonon line. This energy is similar to the energy of the totally symmetric stretching mode ν_1 ν_s(Pr-Cl): 282 cm^{-1} in the 20-K Raman spectrum. The corresponding bands are at slightly lower (ca. 380 cm^{-1}) energy in the spectrum of $Cs_2NaYCl_6:Pr^{3+}$, Fig. 2(b), than in that of $Cs_2NaPrCl_6$, Fig. 2(a). In summary, it is not possible to make definitive assignments for these weaker bands near 200 nm at this stage, although our calculations show that they are unlikely to be associated with $4f^2 \rightarrow 4f^1 5d^1$ transitions. Several alternatives need to be explored, even including charge transfer from chloride $3s$ or $3p$ orbitals.

The extent of overlap of charge-transfer bands with others, due to the $4f^2 \rightarrow 4f^1 5d^1$ transitions, is unclear at present. The relative intensities of features [Figs. 2(a) and 2(b)] which have maxima in the excitation spectra near 60 800 cm^{-1} in $Cs_2NaPrCl_6$ and at 57 500 cm^{-1} in $Cs_2NaYCl_6:Pr^{3+}$ are stronger in the former spectrum. With a $5d$ B_0^4 crystal field parameter (CFP) fixed at the Ce^{3+} value, electronic lines are calculated at 61 954, 62 603, 63 935, and 64 400 cm^{-1} due to $(\Gamma_{1g} \rightarrow \Gamma_{4u})$ $4f^2 \rightarrow 4f^1 5d^1$ transitions, which are 0.55, 0.33, 0.18, and 0.21 times as strong as the strongest line [refer to Sec. IV C and Fig. 9(a)]. However, these calculated relative intensities are applicable to absorption and not to excitation spectra. The comparison with other studies shows that a band is apparent in the spectrum of $Cs_2LiLaCl_6:Ce^{3+}$, at 56 000–60 500 cm^{-1} at 300 K.[42] Park and Oh[43] state that the charge-transfer energy for a ligand p orbital to an unoccupied La^{3+} $4f$ orbital in $LaCl_3$ is 86 300 cm^{-1} and that the value is similar for other Ln^{3+} ions. However, Ionova *et al.*[44] have assigned the lowest $\pi \rightarrow f$ charge-transfer transition of $PrCl_6^{3-}$ at ca. 53 000 cm^{-1}.

To high energy of 100 nm (100 000 cm^{-1}), there is a continuous increase in absorption, which represents the onset of transitions in the $CsCl_{12}$ cluster, from the $5p$ Cs core level to the conduction band.[45,46] The $4f^2$ $[^3H_4]$ $\Gamma_{1g} \rightarrow 4f^1 6p^1$ pure electronic transitions are electric dipole forbidden and vibronically allowed. The $4f^1 5g^1$ configuration is calculated to be at 205 000 cm^{-1} above $4f^2$.

Figures 2(a) and 2(b) also show the 8-K emission spectra of (a) $Cs_2NaPrCl_6$ and (b) $Cs_2NaY_{0.99}Pr_{0.01}Cl_6$, excited by 114-nm synchrotron radiation. The emission bands are similar to those in Fig. 1(a), except that the $4f^1 5d^1 \rightarrow 4f^2$ $[^3H_4]$ transition is clearly observed. No further emission bands were observed using 197.9 nm laser excitation. The decay of the emission at 300 nm was measured at 8 K under 120- or 230 nm excitation and could be fitted by a single exponential [as shown in Figs. 2(c) and 2(d)], indicative of a transition occurring within a single emissive center. The lifetimes were fitted as 13 ns for $Cs_2NaPrCl_6$ and 18 ns for $Cs_2NaY_{0.99}Pr_{0.01}Cl_6$. The lower value for the neat material is attributed to concentration quenching, which is nearly resonant:

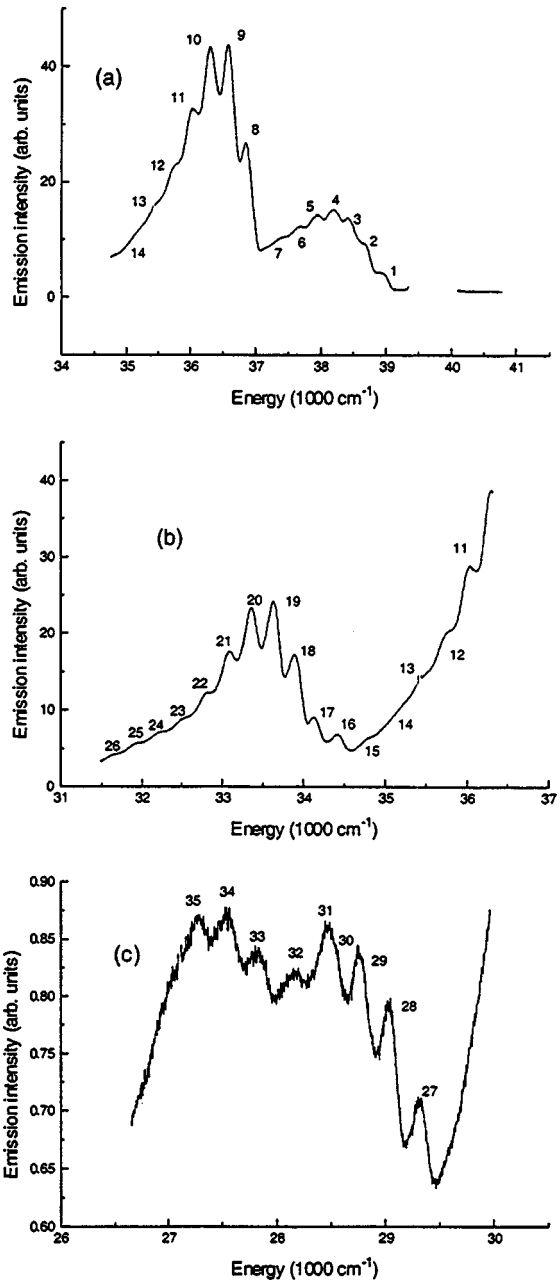

FIG. 3. (a)–(c) 252.7-nm laser excited 10-K emission spectrum of $Cs_2NaPrCl_6$ between 39 500 and 26 500 cm^{-1}. Band numbers are identified in Table I.

$$\Gamma_{3u} 4f^1 5d^1(\text{site } 1) + {}^3H_4 4f^2(\text{site } 2) \rightarrow {}^1I_6 4f^2(\text{site } 1) + {}^1D_2 4f^2(\text{site } 2) + \text{phonon}. \quad (2)$$

B. $4f^1 5d^1 \rightarrow 4f^2$ emission spectra of $Cs_2NaPrCl_6$

The $4f^1 5d^1 \rightarrow 4f^2$ emission spectrum of $Cs_2NaPrCl_6$ was studied at higher resolution at 10 K, Figs. 3(a)–3(c), and similar spectra were obtained under 252.7 nm (39 561 cm^{-1}) and 245.9 nm (40 655 cm^{-1}) laser excitation, but not under 266.0 nm (36 583 cm^{-1}) or 273.9 nm (36 499 cm^{-1}) excitation, since the latter energies are too low to populate the $4f^1 5d^1$ levels. In the former cases, the transition from the

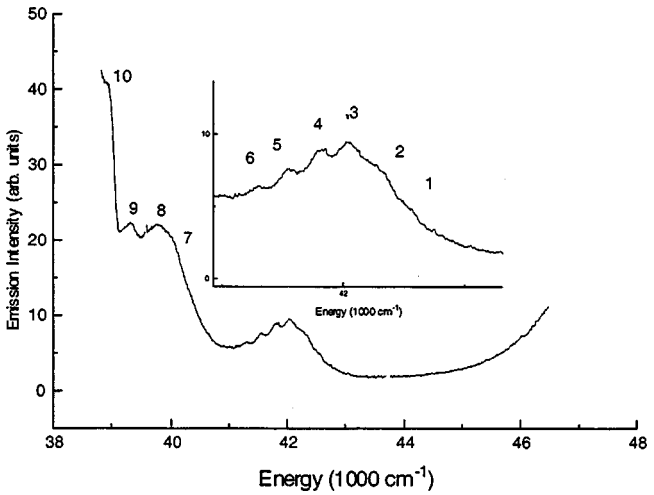

FIG. 4. Highest-energy group of bands in the 208.8-nm laser excited 10-K emission spectrum of $Cs_2NaPrCl_6$. The inset shows more detail in the region between 41 500 and 42 500 cm^{-1}.

lowest $4f^15d^1$ level to the $4f^2$ $[^3H_4]$ term is clearly observed as a structured band, with the first two groups of bands, Fig. 3(a), corresponding to the transitions to the terminal $^3H_4$ and $^3H_5$ levels. The highest-energy group is located near 38 972 cm^{-1}. The mean spacing interval of bands 1–14 is 277 cm^{-1}, which within the accuracy of measurement is similar to energy of the totally symmetric Pr-Cl stretching mode in the ground electronic state. However, from the individual band energies it is not possible to assign specific transitions to individual terminal $4f^2$ crystal field levels, even considering alternative assignments of band 1 to the different crystal field levels of $^3H_4$. The reason for this is that the spectra are not sufficiently well resolved and consist of an unknown number of overlapping bands (cf. Sec. III C), just as in the case of $LiYF_4:Pr^{3+}$.[32] Similar comments also apply to Figs. 3(b) and 3(c), which show the transitions to higher $4f^2$ terminal levels. The bands are associated with different terminal *SLJ* multiplets and are identified in Table I.

Under higher-energy laser excitation at 10 K (using 192.2, 204.2, 208.8, and 223.1 nm excitation) some additional structure is present in the emission spectrum of $Cs_2NaPrCl_6$, with the highest-energy group of bands located near 42 000 cm^{-1}. The highest-energy band (line 1, Fig. 4) is at 42 558 cm^{-1}, and the mean interval separating lines 1–6 is 254 cm^{-1}, which represents a progression in a totally symmetric vibrational mode in an allowed electronic transition. No other lanthanide ion exhibits $4f^{N-1}5d^1 \rightarrow 4f^N$ emission in this spectral region, so that these bands are assigned to further Pr^{3+} site(s), involving transitions to terminal $^3H_4$ levels. Another group of bands (lines 7–9) is evident below 2465 cm^{-1} to low energy, presumably associated with transitions to $^3H_5$, but further structure is absent or masked by the emission shown in Fig. 3. The situation is analogous to the $5d \rightarrow 4f$ emission spectra of Ce^{3+}, where additional bands have been observed and assigned either to crystal disorder or to the intergrowth of a second phase.[25] Luminescence does not occur from crystal field levels with energy gaps spanned by fewer than five phonons (as would be the case for a level at 42 558 cm^{-1}) unless specific restrictive nonradiative selection rules are applicable.[47] Thus it is clear from our energy level calculations (Sec. IV) that the emission does not originate from a further $4f^15d^1$ excited state of Pr^{3+} in octahedral symmetry $PrCl_6^{3-}$. Since analogous emission bands are also present in the spectra of $Cs_2NaYCl_6:Pr^{3+}$ and $Cs_2LiPrCl_6$, it is presumed that the luminescent Pr^{3+} center is located at a defect site (next to hydroxide or oxychloride ions) or at a different crystal site (such as replacing Cs^+ in the $CsCl_{12}$ cluster).

C. $4f^15d^1 \rightarrow 4f^2$ emission spectra of $Cs_2NaYCl_6:Pr^{3+}$

Figure 5 shows the 10-K $4f^15d^1 \rightarrow 4f^2$ emission spectrum of Pr^{3+} diluted into cubic Cs_2NaYCl_6. Similar spectra were obtained under 252.7 and 223.1 nm excitation, which also extend into the orange spectral region, Fig. 5(e). Notably, the transitions to individual crystal field levels can be clearly resolved and the locations of zero-phonon lines can be deduced. The latter are marked by line numbers (Fig. 5), which are listed in Table II. Consideration of the spacing intervals between the different groups of bands enables the terminal $4f^2$ level of the highest-energy transition to be assigned to $[^3H_4]$ Γ_{4g}.[34] Then, the derived energies of the other terminal crystal field levels are listed in Table II, and the comparison with the $4f^2$ crystal field levels deduced from the $^3P_0$ emission and excitation spectra[8] is included. Note that the latter are more accurately determined than in the present determinations, due to the calibration errors and subtraction of two large quantities. The transitions to the higher $4f^2$ levels, Fig. 5(e), are generally very weak (see Sec. IV D) and overlapped by $4f^2$-$4f^2$ emission or absorption transitions, so that the assignments are then less certain. It is clear, however, that selection rules operating for the $4f^15d^1 \rightarrow 4f^2$ emission transitions restrict the terminal state representations Γ_f only to Γ_{4g} and Γ_{5g}. For an electric-dipole-allowed transition, the product of the initial and final crystal field level representations must contain the representation of the dipole moment operator, which is Γ_{4u} in octahedral symmetry. The lowest $4f^15d^1$ state (at 39 017 cm^{-1}) therefore corresponds to the Γ_{3u} representation.[34]

Each electronic transition in $Cs_2NaYCl_6:Pr^{3+}$ comprises progressions in at least two vibrational modes: the ν_1(Pr-Cl) stretch with energy 298 cm^{-1} and a lattice mode with energy 48 cm^{-1}, which is discussed in the following Sec. III E. Some of these intervals are marked in Fig. 5, with each terminal crystal field state also being indicated. The progression intervals are fairly constant for successive members, so that the $4f^2$ potential energy systems can be regarded as harmonic. The ground-state vibrational energies of $Cs_2NaPrCl_6$, from infrared, vibronic, and Raman data, are compared with calculated values from the simple moiety mode and unit cell group models in Table III. There are, however, some changes in vibrational energies for the Pr^{3+} ion situated at the Y^{3+} site in Cs_2NaYCl_6. Doping Pr^{3+} into Cs_2NaYCl_6 stretches the lattice constant by 1.6%,[51] and for example, the ν_1(Pr-Cl) frequency increases by 7.6%.[49] The ionic radius of Y^{3+} in Cs_2NaYCl_6 is close to that of Er^{3+} in

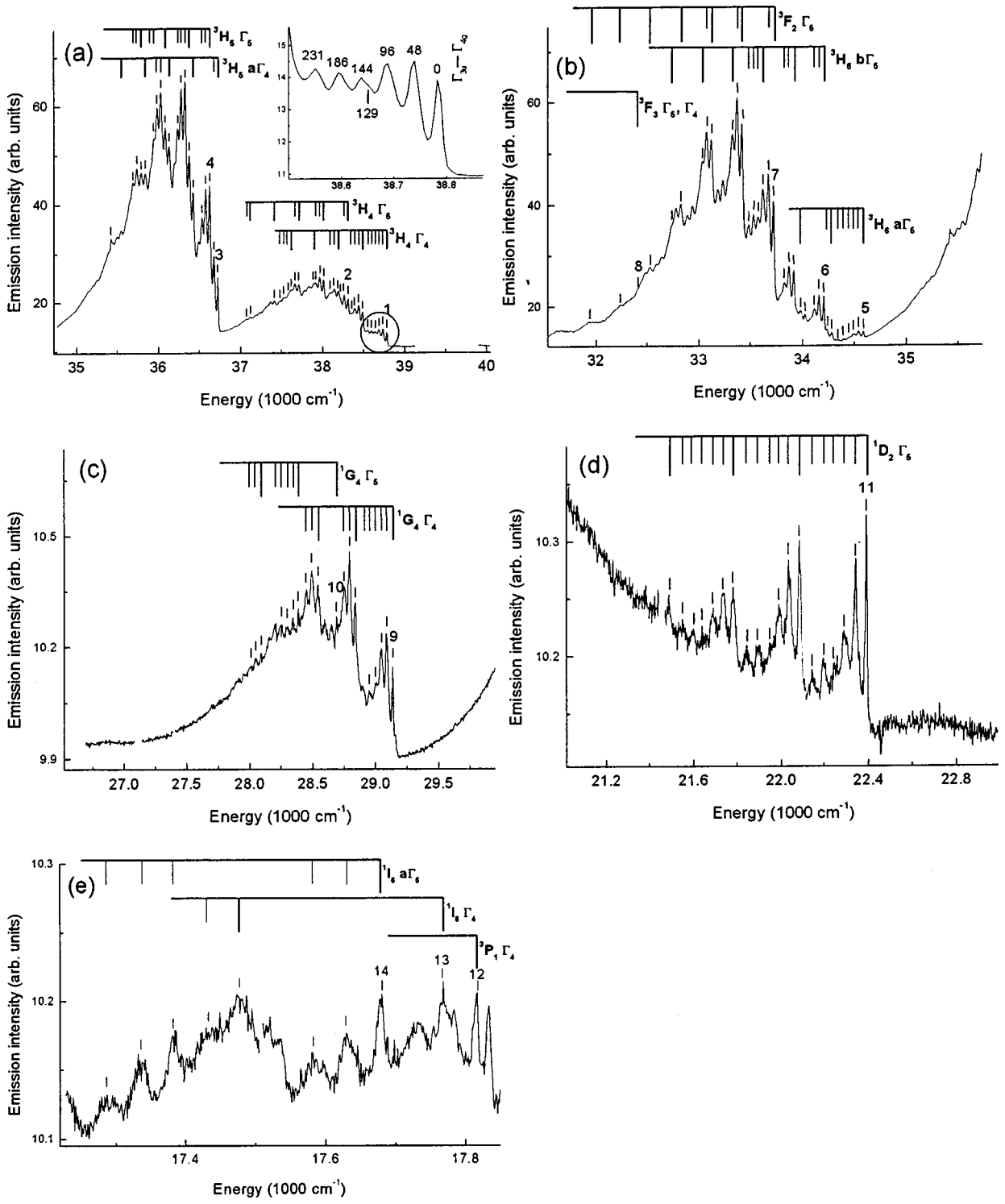

FIG. 5. (a)–(e) 252.7-nm excited 10-K emission spectrum of $Cs_2NaY_{0.99}Pr_{0.01}Cl_6$ between 40 000 and 16 800 cm^{-1}. The progressions in ν_1 and in the lattice mode are indicated. Zero-phonon lines are assigned to terminal *SLJ* states, and the numbers correspond to levels in Table II. The inset in (a) shows the first (circled) group of bands in greater detail, with the displacements from the $\Gamma_{3u}\rightarrow\Gamma_{4g}$ origin marked.

$Cs_2NaErCl_6$,[51] so the vibrational data of the latter system are also included in Table III for comparison.

D. $4f^15d^1\rightarrow 4f^2$ emission spectra of $Cs_2LiPrCl_6$

The 10-K $4f^2$ absorption spectrum of $Cs_2LiPrCl_6$ shows that the $PrCl_6^{3-}$ moiety exhibits a slight distortion from O_h point group symmetry at this temperature. Nevertheless, the 252.7-nm excited $4f^15d^1\rightarrow 4f^2$ emission spectrum of $Cs_2LiPrCl_6$ at 10 K (Fig. 6) is more clearly resolved than that of $Cs_2NaPrCl_6$. In this case the luminescent Γ_{3u} state is inferred to be at 39 096 cm^{-1}. The derived $4f^2$ energy levels are also collected in Table II. The major progression-forming

TABLE II. Derived energies of electronic states observed in the 10-K $4f^15d^1 \rightarrow 4f^2$ emission spectra of $Cs_2NaYCl_6:Pr^{3+}$ and $Cs_2LiPrCl_6$.

				Relative intensity			
$4f^2$ level $SLJ\gamma\Gamma$	Energy (cm^{-1}), $Cs_2NaYCl_6:Pr^{3+}$ (Ref. 8)	Line, Fig. 5	Derived energy[b] (cm^{-1}) $Cs_2NaYCl_6:Pr^{3+}$	Obs.	Calc.	Line, Fig. 6	Derived energy[b] (cm^{-1}) $Cs_2LiPrCl_6$
$^3H_4\Gamma_4$	245	1	245	1.00	1.00	1	234
$^3H_4\Gamma_5$	721	2	719	1.1	0.70	2	702
$^3H_5a\Gamma_4$	2300	3	2302	2.7	0.38	3	2296
$^3H_5\Gamma_5$	2404	4	2400	11.6	1.28	4	2389
$^3H_5b\Gamma_4$	2748			n.o.	0.002		
$^3H_6a\Gamma_5$	4438	5	4442	0.36	0.13	5	4431
$^3H_6b\Gamma_5$	4811	6	4816	2.4	0.66	6	4807
$^3H_6\Gamma_4$	4886			n.o.	0.08		
$^3F_2\Gamma_5$	5303	7	5306	7.5	2.41	7	5289
$^3F_3\Gamma_4,\Gamma_5$	6619	8	6613	<0.15	0.14		
$^3F_4\Gamma_4$	7010			n.o.	0.009	8	6991?
$^3F_4\Gamma_5$	7281			n.o.	0.022		
$^1G_4\Gamma_4$	9899[a]	9	9886	0.05	0.00002	9	9885
$^1G_4\Gamma_5$	10325[a]	10	10337	0.03	0.00008		
$^1D_2\Gamma_5$	16647	11	16634	0.03	0.003		
$^3P_1\Gamma_4$	21197	12	21207	0.015			
$^1I_6\Gamma_4$		13	21225?	0.004			
$^1I_6a\Gamma_5$		14	21343?	0.02			
$^1I_6b\Gamma_5$	21974			n.o.			
$^3P_2\Gamma_5$	22347	15	22337	0.002			

[a]From $Cs_2NaPrCl_6$.

[b]The air-to-vacuum calibration is about 12 cm^{-1} in the ultraviolet region, and the spectral resolution employed was 4 cm^{-1}. The directly determined energies from Ref. 8 are more accurate than the derived energies from the subtraction of two large energies in the present case.

vibrational mode in the emission spectra of $Cs_2LiPrCl_6$ is the totally symmetric ν_1(Pr-Cl) stretch, in this case with energy 289 cm^{-1}.

E. Vibronic structure

The lower-energy vibrational structure in the absorption and emission spectra of $Cs_2NaYCl_6:Pr^{3+}$ is shown in greater detail in the insets of Figs. 5(a) and 7(e), and the vibrational displacements are summarized in Table III.

The selection rule for a progression-forming mode, η, in an allowed electronic emission transition at low temperatures, when upper level vibrational levels are not populated, is that Γ_η contains Γ_{1g}. The Cl^- ions are the first-nearest neighbors of Pr^{3+} ions, situated at a distance of 0.246**a**, where **a** is the unit cell lattice parameter. The totally symmetric ν_1(Pr-Cl) stretch is thus the strongest progression-forming mode in the $4f^2 \leftrightarrow 4f^15d^1$ vibronic sidebands. The appearance of a second progression in the emission spectrum is unexpected, since there is only one totally symmetric vibrational mode for the unit cell of the elpasolite-type lattice. The lattice mode progression has the interval 50 ± 3 cm^{-1} in $Cs_2LiPrCl_6$, compared with 47 ± 2 cm^{-1} in the emission spectrum of $Cs_2NaYCl_6:Pr^{3+}$. This lattice mode progression has been observed in other electric dipole allowed transitions, however, with the corresponding energy in the $4f^1 \rightarrow 5d^1$ absorption spectrum of $Cs_2NaYCl_6:Ce^{3+}$ being 46 cm^{-1}.[22] In the latter case the vibrational mode was assigned to a localized or pseudolocalized α_{1g} symmetry lattice mode, following previous studies of rare-earth ions diluted into host crystals.[52,53] The corresponding energy in our (unpublished) $5f^3 \rightarrow 5f^26d^1$ 10-K absorption spectrum of $Cs_2NaYCl_6:U^{3+}$ is 45 ± 2 cm^{-1}. Therefore neither the rare-earth ion nor the Na/Li nuclei are significantly involved in this vibrational motion. The fact that the vibration is observed in the spectrum of *neat* $Cs_2LiPrCl_6$ shows that it is not a localized mode. The nuclear motion clearly involves Cs^+, but although the $\mathbf{k}=0$ unit cell group mode with Cs^+ motion observed in the Raman spectrum has a similar energy, it corresponds to $\tau_{2g}(O_h)$ symmetry. The lattice vibration is therefore assigned to a zone-boundary mode, such as along the Δ direction of the reciprocal lattice space. An alternative, but less accurate description (since it ignores couplings between Pr^{3+} ions and with other shells) is that the vibration corresponds to totally symmetric breathing of the second shell, $PrCs_8$.

Following the assignments of bands to the first two shells of the Pr^{3+} ion, and taking the **G** and **F** matrix elements of the general valence force field for MX_6 and MX_8 systems in

TABLE III. Vibrational energies of $Cs_2NaPrCl_6$ and $Cs_2NaErCl_6$. TO/LO transverse/longitudinal optic modes; str. stretch; sym. symmetric; ant. antisymmetric; trans. translatory.

Unit cell group mode (Ref. 48) and O_h point group irrep	Moiety mode and O_h point group irrep	20-K Raman spectrum $Cs_2NaPrCl_6$	90-K $4f^2$-$4f^2$ vibronic spectra $Cs_2NaPrCl_6$	Calc.[a]	Calc.[b]	$Cs_2NaErCl_6$ 20-K Raman and 10-K $4f^{11}$ vibronic spectra	$PrCl_6^{3-}$ in Cs_2NaYCl_6 $4f^2 \leftrightarrow 4f5d$ spectra at 10 K[c]
S_1 Pr-Cl sym. str.	$\nu_1(\alpha_{1g})$	282		282	282	298	298±4
S_2 Pr-Cl str.	ν_2 (ε_g)	221		221	221	236	(231)
S_3 rotatory lattice (τ_{1g})			~20		21		
S_4 Cl-Pr-Cl bend	ν_5 (τ_{2g})	115		112	116	126	(128)
S_5 Cs transl. (τ_{2g})		46			47	58, 69	48
S_6 Pr-Cl ant. str.	ν_3 (τ_{1u})		245(TO); 276(LO)	255	251	259, 286	
S_7 Cl-Pr-Cl bend	ν_4 (τ_{1u})		98(TO); 120(LO)	105	110	108, 116, 131	
S_8 Na-Cl str. (τ_{1u})			173		163	182	(186)
S_9 Cs transl. (τ_{1u})			60(TO)		52	47	
S_{10} Cl-Pr-Cl bend	ν_6 (τ_{2u})		72–82	79	76	78, 86	

[a]Using a five-parameter general valence force field model for moiety modes, Ref. 49.

[b]Using a nine-parameter unit cell group model, Ref. 50.

[c]Refer to Sec. III E for a discussion of the assignments. The modes are totally symmetric, with the exception of S_2 and S_4, which are very weak.

$Cs_2NaYCl_6:Pr^{3+}$,[54,55] with reasonable assumptions about bond-bond interaction constants, then the principal stretching force constants (in $N\,m^{-1}$) are 119 and 9.6 for the first two shells.

The corresponding vibration of the third shell, $PrNa_6$, can then be assigned to a band located between 177 and 193 cm^{-1} to low energy of each of the zero-phonon lines in the $4f^15d^1 \rightarrow 4f^2$ emission spectra of $Cs_2NaYCl_6:Pr^{3+}$. The vibration energy of ca. 186 cm^{-1} does not coincide with any of the $PrCl_6^{3-}$ moiety mode energies, but is similar to the energy of the S_8 ''sodium'' unit cell group mode (Table III). The first member of the progression of this ''sodium'' mode upon the zero-phonon line (i.e., at ca. 186 cm^{-1}) is narrower and more intense than the neighboring third member of the Cs^+ lattice mode progression, showing clearly that it does gain all of its intensity from the fourth member (i.e., $4 \times 47\ cm^{-1}$). Additional vibronic intensity arises in the spectral region of the feature near 186 cm^{-1} due to (i) the first member of a progression (in the Cs^+ lattice mode) upon the progression in the internal τ_{2g} mode upon the zero-phonon line (i.e., $47+128=175\ cm^{-1}$) and (ii) the first member of the progression in an even number of quanta of the Cl-Pr-Cl bending mode upon the zero-phonon line (i.e., $2\times96 = 192\ cm^{-1}$).

There is no evidence for *prominent* Jahn-Teller effects involving the τ_{2g} or ε_g modes from the emission spectra, although weak progressions in these modes could be obscured by the stronger totally symmetric mode progressions. Bands in the absorption spectrum of $Cs_2NaYCl_6:Ce^{3+}$ were located near 194 and 234 cm^{-1} above the zero-phonon line and were assigned to the $\nu_2(\varepsilon_g)$ mode and the fifth member of the lattice mode progression respectively,[22] since the vibrational modes of $CeCl_6^{3-}$ were not well characterized at that time. We have assigned the $\nu_2(\varepsilon_g)$ vibration at 222 cm^{-1} (236 cm^{-1}) in the 20-K Raman spectra of $Cs_2NaCeCl_6$ ($Cs_2NaErCl_6$).[10] The feature observed in the emission and absorption spectra of $Cs_2NaYCl_6:Pr^{3+}$ near 231 cm^{-1} could thus gain intensity from the first member of the ν_2 progression upon the zero-phonon line (as well as $47+186\ cm^{-1}$). The energy of a weak (shoulder) band at 129 cm^{-1} to low energy of the zero-phonon line in the emission spectra of $Cs_2NaYCl_6:Pr^{3+}$ is close to that of the $\nu_5(\tau_{2g})$ vibration (Table III). The analogous feature is more clearly resolved (at 128 cm^{-1} above the zero-phonon line) in the absorption spectrum, Fig. 7(e).

F. $4f^2 \rightarrow 4f^15d^1$ absorption spectra of $Cs_2NaYCl_6:Pr^{3+}$

The first groups of bands in the 10-K absorption spectrum of Pr^{3+} diluted into Cs_2NaYCl_6 at two different concentrations are shown in Fig. 7. The lowest-energy zero-phonon line, at $39\,792\pm3\ cm^{-1}$, is assigned to the transition from the $4f^2$ $[^3H_4]$ Γ_{1g} ground state to the first Γ_{4u} level of the $4f^15d^1$ configuration. Based upon this electronic origin, the vibrational progression energies are marginally less than those observed in the $4f^15d^1 \rightarrow 4f^2$ emission spectra, so that the participation of the $4f$ electrons in bonding is very small, and the ionic model of the $PrCl_6^{3-}$ moiety appears to be a good approximation. Altogether, there are a further 17 Γ_{4u} levels of the $4f^15d^1$ configuration at higher energy. Due to the complexity of the absorption spectrum, the overlapping of bands, and our instrument cutoff, only a few further excited Γ_{4u} levels can be conclusively identified. The relevant zero-phonon lines are marked by arrows in Fig. 7(a), and each heralds the commencement of further vibrational progressions. The first of these electronic origins is at 40 343

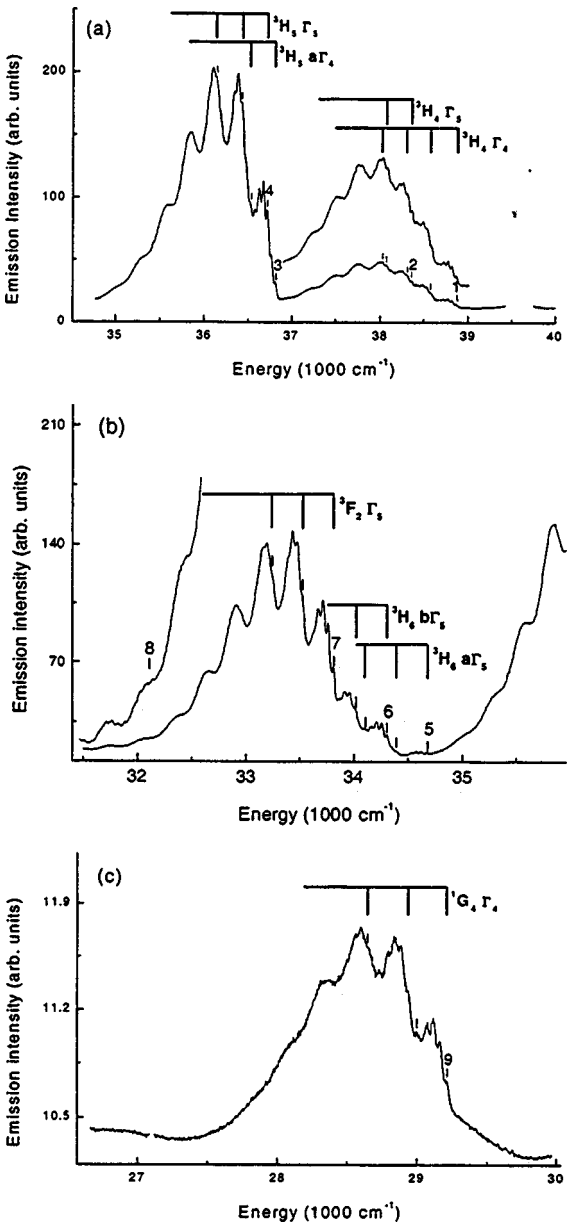

FIG. 6. (a)–(c) 252.7-nm excited 10-K emission spectrum of $Cs_2LiPrCl_6$ between 40 000 and 27 000 cm^{-1}. The progressions in ν_1 and in the lattice mode are indicated. Zero-phonon lines are assigned to terminal *SLJ* states, and the numbers correspond to the levels in Table II.

cm^{-1}, overlapping with the progressions upon the lowest-energy electronic origin. To higher energy, a new feature observed at 41 940 cm^{-1}. It is accompanied by another new weak band at 51 ± 3 cm^{-1} to low energy (i.e., at 41 889 cm^{-1}), which does not correspond to a ''hot'' transition. A new series of lines also commences at 43 711 cm^{-1}. Finally, the assignment of a further electronic origin is uncertain at either 40 804 or 41 110 cm^{-1}. Thus, at most, only five or six Γ_{4u} levels can be assigned.

To low energy of the first absorption transition, the spectrum is complicated by the superposition of absorption and emission bands. Electronic origins are clearly identified at 10 K, at lower energy than shown in the spectrum of Fig. 7(a),

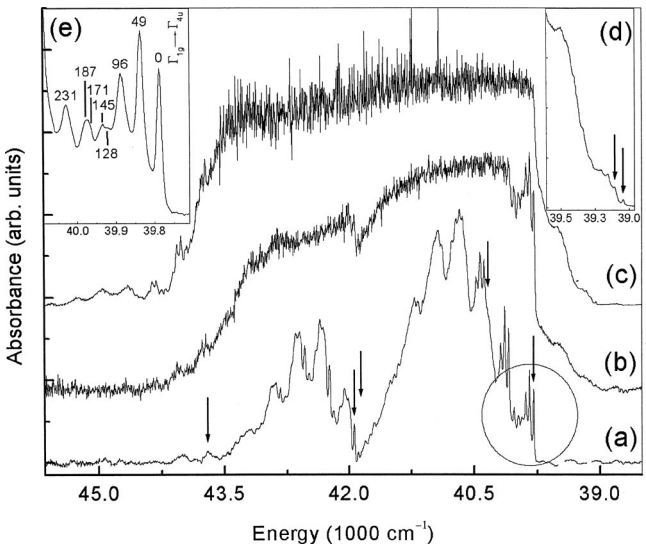

FIG. 7. 10-K absorption spectrum of $Cs_2NaYCl_6:Pr^{3+}$ between 39 000 and 45 000 cm^{-1}. (a) 0.01 mol %, (b), (c) 0.5 mol %, but polished thinner for (b). (d) shows the onset of absorption in (c) on an expanded scale. (e) shows the first (circled) group of bands in (a) in greater detail, with the displacements from the $\Gamma_{1g}\rightarrow\Gamma_{4u}$ zero-phonon line marked. The instrument response is poor above 45 000 cm^{-1}. Electronic origins are indicated by arrows.

at 38 764 and 38 289 cm^{-1}, which correspond to the $\Gamma_{3u}\rightarrow\Gamma_{4g}$, Γ_{5g} emission transitions, respectively. At lower energy, the ν_1 and ν(lattice) mode progressions are based upon these origins. The spectral features broaden rapidly and are obscured above 10 K, so that the observation of hot bands is not possible. However, since the 10-K spectrum, Fig. 7(c), exhibits total absorption, some very weak, low-energy absorption bands, shown in the inset Fig. 7(d), are assigned to hot bands. Two transitions are identified [with the electronic origins shown by arrows in Fig. 7(d)] which can account for all of the observed bands. The zero-phonon lines are located at 39 048 and 39 109 cm^{-1} and are assigned to the $[^3H_4]$ $\Gamma_{4g}\rightarrow\Gamma_{5u}$, Γ_{1u} hot transitions, so that the Γ_{5u} and Γ_{1u} levels are located at 39 293 and 39 354 cm^{-1}. Although the assignments for these very weak bands are tentative, we are unable to provide alternative explanations for their occurrence.

The first few bands of the vibrational structure based upon the $\Gamma_{3u}\rightarrow\Gamma_{4g}$ zero-phonon line are shown in detail in Fig. 7(e), and the bands are assigned analogously to those in the emission spectrum, Sec. III E.

G. Stokes shift and Franck-Condon pattern

The term ''Stokes shift'' [56] strictly applies to the difference in energy between the absorption and emission intensity maxima, when the emission and absorption zero-phonon lines of an electronic-vibrational system are coincident, and there is one progression-forming mode in the allowed transition. It is usually vaguely employed, however, as the separation between the intensity maxima in the absorption and emission spectra. The relevant spectra for the case of $PrCl_6^{3-}$ are shown in Fig. 8, and there are two factors re-

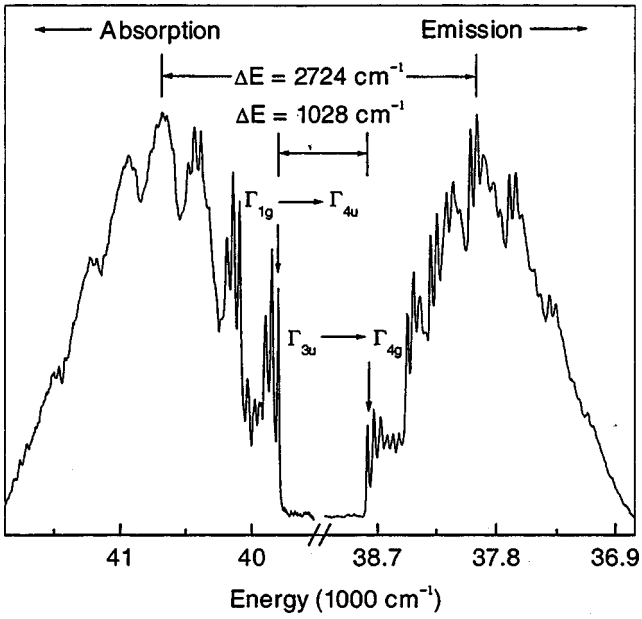

FIG. 8. Comparison of 10-K absorption and emission spectra of $Cs_2NaYCl_6:Pr^{3+}$.

sponsible for the large gap between the peaks of the absorption and emission spectra. First, the small change in Pr-Cl bond length from the $4f^2$ to $4f^15d^1$ configurations leads to an intensity maximum at the first member of the $n\nu_1$ vibrational progression in the absorption and emission spectra. Second, the highest-energy emission and lowest-energy absorption transitions are different, being $\Gamma_{3u}\rightarrow\Gamma_{4g}$ and $\Gamma_{1g}\rightarrow\Gamma_{4u}$, respectively. In addition, further electronic transitions occur in absorption and emission, which serve to destroy the mirror-image relationship between these spectra. The spectral features are more clearly resolved than in other, previously reported $4f^{N-1}5d^1$-$4f^N$ spectra of lanthanide ion systems because (i) the energy level scheme comprises highly degenerate levels in this octahedral symmetry system and (ii) the selection rules are particularly restrictive in octahedral symmetry. Thus, in systems such as YAG:Pr^{3+}, where all electronic energy levels are nondegenerate and all transitions are electric dipole allowed (at the D_2 site symmetry of Pr^{3+}) between the $4f^2$ and $4f^15d^1$ crystal field states, the overlapping of bands gives rise to broad, unresolved features. Furthermore, in such noncentrosymmetric systems, not only are there more pure electronic transitions, but also vibrational progressions are based upon each of the electronic origins. The $4f^{N-1}5d^1$-$4f^N$ spectra of Ln^{3+} in elpasolite lattices are also broad and unstructured at higher temperatures, because many ''hot'' transitions, originating from excited crystal field levels of the ground state *SLJ* term, can then acquire intensity.

The major vibrational progressions in the emission spectra involve the totally symmetric lanthanide-chloride stretching mode. Fits to the intensities $I_{0,n}$ $(n=1,...)$ of the $n\nu_1$ ν_s(Pr-Cl) progression upon the zero-phonon line in emission were utilized to calculate the ratios of overlap integrals:[57]

$$\frac{I_{0,n}}{I_{0,0}}=\left[\frac{E(\mathrm{ZPL})-n\overline{\nu_1}}{E(\mathrm{ZPL})}\right]^4\left[\frac{\langle 0|n\rangle}{\langle 0|0\rangle}\right]^2, \tag{3}$$

where $E(\mathrm{ZPL})$ is the zero-phonon-line energy, and $n\overline{\nu_1}$ is the energy of n quanta of $\nu_1\nu_s$(Pr-Cl). The corresponding formula for the absorption spectra is[57]

$$\frac{I_{n,0}}{I_{0,0}}=\left[\frac{E(\mathrm{ZPL})+n\overline{\nu_1}}{E(\mathrm{ZPL})}\right]\left[\frac{\langle n|0\rangle}{\langle 0|0\rangle}\right]^2. \tag{4}$$

This formula neglects the changes in bulk refractivity and effective field correction[58] with energy, which is justifiable in the present case for the change in energy of <3000 cm^{-1}. The overlap integrals $\langle n|0\rangle$ and $\langle 0|0\rangle$ may also be calculated from recursion formulas[59] involving a dimensionless Franck-Condon offset parameter and the angle θ, derived from the ratio of excited state (e) and ground state (g) frequencies, given by

$$\tan\theta=\left[\frac{\overline{\nu_1}\nu_s(\mathrm{Pr\text{-}Cl})_e}{\overline{\nu_1}\nu_s(\mathrm{Pr\text{-}Cl})_g}\right]^{0.5}. \tag{5}$$

Since the frequencies are very similar in the present case, we have simplified the recursion formulas by taking $\tan\theta=1$, so that the Huang-Rhys parameters for the ground and excited states are then equal. In that case,[57]

$$\langle 0|0\rangle=\exp(-39.12\Delta S^2), \tag{6}$$

$$\langle n+1|0\rangle=(-25.02\Delta S\langle n|0\rangle)/[8(n+1)]^{1/2}, \tag{7}$$

where ΔS is the displacement (Å) of the minimum of the potential energy surface of the excited $4f^15d^1$ state along the α_{1g} coordinate, relative to a particular $4f^2$ state. The individual Pr-Cl bond length change is given by $\Delta r=\Delta S/\sqrt{6}$. The choice of baseline for the integration of allowed transitions has differed in previous studies,[52,53,57] depending upon whether or not the continuous, underlying background has been substracted, as in this study. For emission, the bands are generally narrowest on the high-energy side of any one transition and broader on the low-energy side.[53] The broad background has been assigned to totally symmetric (lattice) vibrations extending over a larger frequency range than those responsible for the sharp vibronic lines.[53]

The results (ΔS and Δr) from the fittings of progression intensities of both the ν_1(Pr-Cl) and ν(lattice) modes are collected in Table IV. The derived vibrational energies are also included. The displacement Δr is then calculated to be about 0.05 Å, which is $<2\%$ change in Pr-Cl bond distance. The derived progression frequencies for ν_1 appear to be marginally greater for the singlet ($^1D_2$ and $^1G_4$) terms than for the triplet terms of $4f^2$. This is consistent with the greater configurational admixture of p-electron character into the singlet states.[8] The change in Pr-Cs distance from the $4f^2$ to the $4f^15d^1$ configuration is $<1\%$ (Table IV).

IV. ENERGY LEVEL AND INTENSITY CALCULATIONS

A. $4f^2$ and $4f^15d^1$ configurations of $PrCl_6^{3-}$: Energy levels and wave vectors

The $4f^{N-1}5d^1\rightarrow 4f^N$ transitions are allowed, so that, for any compound, whatever the site symmetry, and to the first

TABLE IV. Progression frequencies and bond length changes in the $4f^2$-$4f^15d^1$ spectra of Pr^{3+} in elpasolite hosts. Refer to Sec. III G for definitions of ΔS and Δr.

Crystal host	Pr^{3+} dopant ion concentration	Transition	ν_1 (cm^{-1})	ΔS_1 (Å)	Δr_1 (Å)	ν(lat) (cm^{-1})	ΔS(lat) (Å)	Δr(lat) (Å)
Cs_2NaYCl_6[a]	1 mol %	$\Gamma_{3u}\rightarrow{}^3H_4\Gamma_{4g}$	296±1	0.14	0.057	48±1	0.16	0.055
		$\Gamma_{3u}\rightarrow{}^3H_5a\Gamma_{4g}$	296±2	0.14	0.057	46±2	0.17	0.060
		$\Gamma_{3u}\rightarrow{}^3H_6a\Gamma_{5g}$	296±2	0.14	0.057	46±2	0.17	0.060
		$\Gamma_{3u}\rightarrow{}^1G_4\Gamma_{4g}$	297±4	0.13	0.055	46±4	0.20	0.068
		$\Gamma_{3u}\rightarrow{}^1D_2\Gamma_{5g}$	302±5	0.12	0.049	46±4	0.15	0.054
$Cs_2LiPrCl_6$[a]	100 mol %	$\Gamma_{3u}\rightarrow{}^3H_4\Gamma_{4g}$	285±3	0.11	0.043	50±3	0.18	0.063
		$\Gamma_{3u}\rightarrow{}^3H_6a\Gamma_{5g}$	282±2	0.10	0.042	50±3	0.19	0.068
		$\Gamma_{3u}\rightarrow{}^3H_6b\Gamma_{5g}$	286±4	0.12	0.047	49±2	0.18	0.066
		$\Gamma_{3u}\rightarrow{}^3F_2\Gamma_{5g}$	288±2	0.10	0.042	51±2	0.19	0.068
		$\Gamma_{3u}\rightarrow{}^1G_4\Gamma_{4g}$	286±1	0.12	0.048	51±5	0.20	0.072
Cs_2NaYCl_6[b]	0.01 mol %	${}^3H_4\Gamma_{1g}\rightarrow\Gamma_{4u}$[c]	293±3	0.14	0.057	47±4	0.15	0.055
		${}^3H_4\Gamma_{1g}\rightarrow\Gamma_{4u}$[d]	294±3	0.13	0.056			

[a]Emission spectrum.
[b]Absorption spectrum.
[c]39 792±3 cm^{-1}.
[d]41 940 cm^{-1}.

order, the calculation of the $4f^15d^1\rightarrow4f^2$ electric dipole transitions requires no knowledge of the degree of mixing of each configuration with an external one of opposite parity. By contrast, this is essential for the forbidden $4f^2\rightarrow4f^2$ transitions. The calculation of $4f^15d^1\rightarrow4f^2$ intensities requires only the composition of the wave vectors of the initial and final states, and involves three steps: (i) the analysis of the ground $4f^2$ configuration, (ii) the simulation of the $4f5d$ configuration with the determination of its electronic-wave functions and (iii) the direct calculation of the intensities.

The parameters defining the $4f^2$ configuration were fitted and the relevant wave vectors were precisely determined in a previous study.[8] The energy level scheme was simulated by a configuration-interaction-assisted crystal field (CIACF) calculation, performed within a basis set including the $4f^2$ as well as one or more excited configurations. In the case of Pr^{3+}, the inclusion of $4f6p$ was efficient in significantly improving the agreement between calculated and experimental energy levels. For $PrCl_6^{3-}$, 39 out of 40 levels of $4f^2$ were measured, and for some of them, the CIACF guided and confirmed the experimental assignments. The final deviation of the crystal field analysis was 11.6 cm^{-1}, which was nearly 3 times less than for the analysis in $4f^2$ alone.[8] The ground configuration of Pr^{3+}, $4f^2$, is composed of seven spectroscopic terms ${}^3P$, ${}^3F$, ${}^3H$, ${}^1S$, ${}^1D$, ${}^1G$, and ${}^1I$ and the excited $4f6p$ configuration of six terms, which are ${}^3D$, ${}^3F$, ${}^3G$, ${}^1D$, ${}^1F$, and ${}^1G$. The following parameters are required to describe the ground configuration: the Slater integrals F^0, F^2, F^4, and F^6; the parameters arising from electrostatic configuration interaction α, β, and γ; the parameters M^k ($k=0,2,4$) accounting for the spin–other-orbit interaction; the spin-orbit coupling constant $\zeta(f)$; and the crystal field parameters (CFP's) $B_0^4(f)$ and $B_0^6(f)$. The additional parameters necessary to describe the excited configuration $4f6p$ and its interaction with $4f^2$ are the interconfiguration parameters R^k, the spin-orbit coupling constant $\zeta(p)$, and the CFP $B_0^4(p)$. Since the site symmetry at the Pr^{3+} site in Cs_2NaYCl_6 is O_h, there are no odd CFP. The wave vectors of $4f^2$ and $4f6p$ contain no admixture with the wave vectors of $4f5d$ since there exists neither electrostatic nor crystal field interactions between both configurations. Actually, $4f^2$ and $4f6p$ on the one hand and $4f5d$ on the other behave independently.

An accurate determination of the composition of the $4f5d$ lowest-emitting level is required in order to evaluate the emission probabilities $4f^15d^1\rightarrow4f^2$, and a precise knowledge of the composition of all the $4f5d$ levels is required for the calculation of $4f^2\rightarrow4f^15d^1$ absorption intensities. Consequently, a complete analysis of the $4f5d$ configuration is necessary, which involves the determination of the whole set of atomic and crystal field parameters. The $4f5d$ energy levels and electronic wave functions are determined by a complete calculation within the 140 states of the configuration. The $4f5d$ configuration includes the ten multiplets ${}^3P$, ${}^3D$, ${}^3F$, ${}^3G$, ${}^3H$, ${}^1P$, ${}^1D$, ${}^1F$, ${}^1G$, and ${}^1H$. The evaluation of the matrix elements is performed using a $|SLJM\rangle$ basis set. The model Hamiltonian used to calculate the matrix elements of the electrostatic, spin-orbit, and crystal field interactions is written as[60,61]

$$H=\sum R^k(l_1,l_2,l_1',l_2')\cdot g^k(l_1,l_2,l_1',l_2',k)+\zeta(l)\cdot A_{so}(l)+\sum B_q^k(l)\cdot C_q^k(l). \quad (8)$$

The first term represents the two-electron free-ion repulsion interaction leading to the ${}^{2S+1}L$ terms. l_1 and l_2 on the one hand and l_1' and l_2' on the other are the orbital moments of the two electrons. The R^k and g^k are parameters and opera-

tors, respectively. Selection rules for the two-electron radial integrals R^k (l_1,l_2,l_1',l_2') are easily deduced by inspection[62] of the matrix elements of g^k (l_1,l_2,l_1',l_2',k) containing the product of the two $3j$ symbols:

$$\begin{pmatrix} l_1 & k & l_1' \\ 0 & 0 & 0 \end{pmatrix} \times \begin{pmatrix} l_2 & k & l_2' \\ 0 & 0 & 0 \end{pmatrix}.$$

The selection rules on k determined by triangular conditions are the following:

$$l_1+l_1'+k \text{ must be even as well as } l_2+l_2'+k; l_1-l_1', l_2-l_2' \leqslant k; l_1+l_1', l_2+l_2' \geqslant k. \quad (9)$$

The only possibilities are R^k (f, d, f, d) with $k=2$, 4 and R^k (f, f, d, d) with $k=1$, 3, 5, hence five adjustable parameters ruling the two-electron interactions within the $4f5d$ configuration. Besides, no two-electron interaction exists between $4f^2$ and $4f5d$, since in that case $l_1+l_1'+k$ and $l_2+l_2'+k$ cannot be simultaneously even. The second term in Eq. (8) is the one-electron spin-orbit interaction for $4f$ and $5d$. The spin-orbit–orbit interaction between different orbitals is weak.[61,63] The third term in Eq. (8) is the crystal field interaction within the $4f5d$ states, where $B_q^k(l)$ is a CFP for an electron with the orbital moment l. There are no CFP's linking $4f$ and $5d$ orbitals in O_h symmetry, so that the relevant CFP's are $B_0^4(f)$, $B_0^6(f)$, and $B_0^4(d)$, with the usual relationships $B_4^4=B_0^4(5/14)^{1/2}$ and $B_4^6=-B_0^6(3.5)^{1/2}$.

There exists a connection between the behaviors of $4f^2$ and $4f5d$ in that the features of $4f5d$ depend to some extent on the values the $4f$ CFP's. The latter were refined in $4f^2$ and the modifications are felt in $4f5d$. It is to be noted that the radial integrals $\langle f|r^k|f\rangle$ computed in $4f5d$ are somewhat lower than in $4f^2$.[64] As a first approximation, we shall assume that the parameters for the $4f$ shell determined earlier in $4f^2$ are relevant for the $4f5d$ configuration. The electronic structure of the $4f5d$ configuration depends therefore on a total of seven unknown independent parameters: five two-electron parameters R^k (f, d, f, d) $(k=2,4)$ and R^k (f, f, d, d) $(k=1,3,5)$, the spin-orbit coupling parameter $\zeta(d)$, and one CFP $B_0^4(d)$. The formulas for the calculation of the electrostatic, spin-orbit, and crystal field interactions between configurations l_1l_2 and $l_1'l_2'$ are given in Ref. 62. Unfortunately, the experimental energy level data for $4f^15d^1$ are sparse, especially when compared with that for $4f^2$,[8] so that the assessment of the parameters of the Hamiltonian is a difficult task. The observations that help in the determination of the unknown parameters are the following. First, the lowest level of the $4f5d$ configuration with respect to $^3H_4[\Gamma_{1g}]$ has been assigned to the Γ_{3u} level at 39 017 cm^{-1} (Sec. III C). Second, the value of $B_0^4(d)$ (42 357 cm^{-1}) found for Ce^{3+} in Cs_2NaYCl_6 (Ref. 22) is assumed to be close to the value for Pr^{3+} and is utilized throughout the calculations. A systematic exploration of the R^1, R^2, R^3, R^4, and R^5 values was undertaken in order to determine the zone where Γ_{3u} was ground level. Starting values evaluated by Cowan's RCN31 program[65] are R^k $(f,d,f,d)=30\,271$ and 15 094 cm^{-1} for $k=2$ and 4 and R^k $(f,f,d,d)=12\,903$, 11 160, and 8691 cm^{-1} for $k=1$, 3, and 5, respectively. The calculated value of $\zeta(d)$ is 1148 cm^{-1}. With these values in the interaction matrix, the first (Γ_{3u}) level settles itself 1688 cm^{-1} above the lowest (Γ_{1u}) level of $4f5d$. Variations of R^1, R^2, R^3, R^4, and R^5 around the initial values reveal the existence of a small area inside which the Γ_{3u} level drops down to the ground level, hardly below a Γ_{1u} and a Γ_{5u} level. The values at the center of the area where Γ_{3u} is ground state are $R^1=10\,322$ cm^{-1}, $R^2=18\,162$, $R^3=11\,160$, $R^4=9056$ cm^{-1}, and $R^5=8691$ cm^{-1}, respectively. In other words, the theoretical values are multiplied by 0.8, 0.6, 1, 0.6, and 1, respectively. Γ_{3u} is never more than 130 cm^{-1} lower than the Γ_{5u} and Γ_{1u} levels which are immediately above. For any variation from this starting set, the Γ_{3u} level has a marked tendency to pop upwards and the energy differences with respect to Γ_{5u} and Γ_{1u} are reduced. For instance, Γ_{5u}-Γ_{3u} is equal to 14 cm^{-1} (so that the lowest Γ_{5u} level would be significantly populated at 10 K) for multipliers equal to 0.8, 0.6, 1, 0.8, and 1, that is, for a 33% increase in R^4, which is then equal to 12 075 cm^{-1} instead of 9056 cm^{-1}. This set represents one extreme limit of the zone where Γ_{3u} is ground level of the excited configuration. The Γ_{3u} position is particularly sensitive to R^2 and R^3 and less sensitive to R^1, R^4, and R^5. We have previously graphically shown the displacement of Γ_{3u} as a function of R^2 and R^3.[34]

The diagonalization of the interaction matrix provides the energy level scheme of the $4f5d$ configuration. The $4f^2$-$4f^15d^1$ gap is adjusted for the ground level to lie at 39 017 cm^{-1}. The levels immediately above Γ_{5u} and Γ_{1u} are located at 39 134 and 39 180 cm^{-1}, respectively, instead of at 39 293 and 39 354 cm^{-1} in the tentative experimental assignment (Sec. III F). The $4f5d$ configuration contains 58 irreducible representations (irreps): $6\Gamma_{1u}+5\Gamma_{2u}+12\Gamma_{3u}+18\Gamma_{4u}+17\Gamma_{5u}$. The conditions are close to the ones for the strong field case since $B_0^4(d)$ is 42 357 cm^{-1}, whereas the strongest of the electrostatic parameters R^2 has been set equal to 18 162 cm^{-1}, with the $5d$ spin-orbit coupling constant $\zeta(d)$ and the CFP $B_0^4(f)$ being nearly an order of magnitude lower. Under the action of the crystal field only, the $5d$ orbitals split into $\Gamma_{5g}+\Gamma_{3g}$ levels (0 and 20 170 cm^{-1}),[22] with Γ_{5g} as the lowest level, and the $4f$ orbitals [with $B_0^4(f)=3435$ cm^{-1}] (Ref. 8) split into $\Gamma_{2u}+\Gamma_{4u}+\Gamma_{5u}$ levels (0, 1041, and 1874 cm^{-1}), with the lowest of these being Γ_{2u}.

The combination of these d and f orbital states gives rise to six levels corresponding to the combinations $[(\Gamma_{5g}+\Gamma_{3g})\times(\Gamma_{2u}+\Gamma_{4u}+\Gamma_{5u})]=[(\Gamma_{5g}\times\Gamma_{2u})+(\Gamma_{5g}\times\Gamma_{4u})+(\Gamma_{5g}\times\Gamma_{5u})+(\Gamma_{3g}\times\Gamma_{2u})+(\Gamma_{3g}\times\Gamma_{4u})+(\Gamma_{3g}\times\Gamma_{5u})]$ at 0 (12), 1041 (36), 1874 (36), 20 170 (8), 21 211 (24), and 22 044 (24) cm^{-1}, respectively, where the numbers between parentheses are the total (spin plus orbital) degeneracies. The orbital label of the ground state is $\Gamma_{5g}\times\Gamma_{2u}=\Gamma_{4u}$. The electron spins have to be taken into account, and since the two electrons are not equivalent, the two states $S=0$ $(^1\Gamma_{1g})$ and $S=1$ $(^3\Gamma_{4g})$ are allowed. Therefore the complete spin $\times$orbital ground-state composition is $(^1\Gamma_{1g}+^3\Gamma_{4g})\times\Gamma_{4u}=^1\Gamma_{4u}+^3\Gamma_{1u}+^3\Gamma_{3u}+^3\Gamma_{4u}+^3\Gamma_{5u}$.

With *all* the interactions switched on, we find for the $4f5d$ configuration, two well-separated sets of 84 (lower) and 56 (upper) levels, respectively, reflecting the $\Gamma_{5g}+\Gamma_{3g}$ decomposition of $5d$ in the cubic crystal field. The total spread of the configuration amounts to 33 600 cm^{-1}, and a gap 8000 cm^{-1} wide separates the upper and lower sets. Within these two sets, the effect of the $4f$ crystal field is blurred by the interelectronic repulsion. The wave vectors are determined as linear combinations of the 140 $|SLJM\rangle$ basis set. This set of wave vectors as well those of $4f^2$ determined previously from the basis set of $4f^2$ states only (dimension 91) and from the enlarged $4f^2+4f6p$ basis set (dimension 175) is all the information necessary to evaluate the absorption and emission intensities.

B. Formulas and selection rules for calculation of intensities

The oscillator strength, f_{ij}, for an electric-dipole-allowed absorption transition from a single lower level i to a single higher level j is written as[61]

$$f_{ij}=3.0376\times10^{-6}\ \Delta E\chi_a\sum_{\rho}S(i,j,p)^2/3, \qquad (10)$$

where $\Delta E=E_j-E_i$ is the transition energy in rydbergs, χ_a the correction factor for the Lorentz effective field and bulk refractivity of the medium [given by $(n^2+2)^2/9n$, where n is the refractive index[58]], and $S(i,j,p)$ is the intensity matrix element between i and j for the p polarization ($p=0,\pm1$). The transition probability for the emission transition $j\rightarrow i$ is given by[61]

$$f_{ji}=2.0261\times10^{-6}(\Delta E)^3\chi_e\sum_{p}S(i,j,p)^2/3, \qquad (11)$$

where the correction factor, χ_e, is $n(n^2+2)^2/9$. The expression for $S(i,j,p)$ in Eqs. (10) and (11) is given by

$$S(i,j,p)=\sum_{M_1,M_2}^{N_1,N_2}\langle M_2|C_p^1|M_1\rangle \times\langle 4f|r^1|5d\rangle z(M_2,N_2)z(M_1,N_1), \qquad (12)$$

where M_2 and M_1 refer to $4f5d|SLJM\rangle$ and $4f^2|S'L'J'M'\rangle$ basis states, respectively, and $z(M_2,N_2)$ and $z(M_1,N_1)$ are the amounts of M_1 and M_2 states in the eigenfunctions N_1 and N_2, respectively. The general expression of the angular part $\langle M_2|C_p^1|M_1\rangle$ for the case of two-electron configurations is given in the Appendix.

For electric dipole electronic transitions, besides the spin selection rule $S=S'$, the other selection rules imposed by the triangular conditions on the product of the $6j$ and $3j$ symbols,

$$\begin{Bmatrix} J & 1 & J' \\ L' & S & L \end{Bmatrix}\times\begin{pmatrix} J & 1 & J' \\ -M_J & q & M_J' \end{pmatrix},$$

are the following: $L=L'\pm1$, $J=J'\pm1$, $J'=L'\pm1$, and $J=L\pm1$. For example, the $^3H\rightarrow{}^3P$ transitions are electric dipole forbidden since H and P states ($L=5$ and 1, respectively) cannot be connected by a rank-1 operator as shown by the triangular conditions.

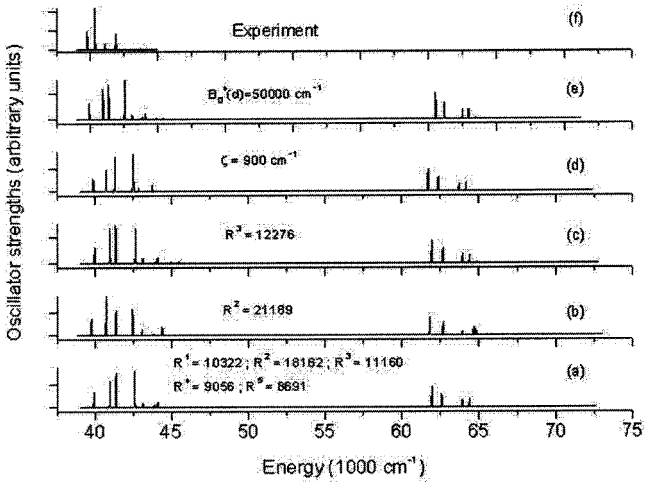

FIG. 9. Simulated $4f^2$-$4f^15d^1$ electronic absorption spectrum of $PrCl_6^{3-}$. The parameter values in (a) are $B_0^4(d)$ 42357 cm^{-1}; $\zeta(d)$ is 1148 cm^{-1}; $R^1=10\,322$ cm^{-1}, $R^2=18\,162$ cm^{-1}, $R^3=11\,160$ cm^{-1}, $R^4=9056$ cm^{-1}, and $R^5=8691$ cm^{-1}. In (b)–(e), one of these parameters is changed, with the others remaining as in (a): $R^2=21\,189$ cm^{-1} in (b), $R^3=12\,276$ cm^{-1} in (c), $\zeta(d)=900$ cm^{-1} in (d), and $B_0^4(d)=50\,000$ cm^{-1} in (e). The gap has been adjusted so that the offset of $4f5d$ is coincident in the six calculations. (f) simulates part of the absorption experimental results, without the vibronic structure.

C. Calculation of the $4f^2\rightarrow4f^15d^1$ absorption strengths

As in the previous fitting of the energy levels in the ground $4f^2$ configuration,[8] the calculation is direct, without approximation, and takes into account the complete $4f5d$ configuration. Since the $4f^2$ ground-state irrep is Γ_{1g} and the electric dipole moment operator behaves as Γ_{4u}, only the transitions terminating upon Γ_{4u} crystal field levels are allowed. The assignments of some absorption transitions of $Cs_2NaYCl_6:Pr^{3+}$ (Fig. 7) have been given in Sec. III F, and the experimental data are presented in a simplified form, showing just the relative intensities of the zero-phonon lines, in Fig. 9(f). Figures 9(a)–9(e) are simulated absorption spectra under various conditions, and the experimental data in the 39 000–45 000 cm^{-1} range are presented. Actually, the six calculated spectra look fairly alike and none of them reproduce exactly the positions and the intensities of the observed experimental peaks. Strong absorption lines correspond to calculated Γ_{4u} levels at 39 918, 40 960, 41 378, and 42 572 cm^{-1} [Fig. 9(e)]. The eigenfunctions of these terminal levels are characterized by large ^3G components. On the other hand, firmly assigned experimental levels occur at 39 792, 40 343, and 41 940 cm^{-1} (Sec. III F). Only the position of the first calculated $\Gamma_{1g}\rightarrow\Gamma_{4u}$ transition matches the experimental one. The observed spectrum seems contracted with respect to the calculated one. Above 42 572 cm^{-1} some weaker transitions are present in the calculated energy level scheme. One of these could be ascribed to an experimentally ob-

served Γ_{4u} level at 43 711 cm^{-1}. The comparison of the simulation with the excitation spectra of $4f^15d^1$-$4f^2$ emission, Figs. 2(a) and 2(b), for the transitions above 60 000 cm^{-1} may be misleading because the excitation spectral intensities not only depend upon absorption strengths, but also upon the efficiency of energy transfer to the emitting level.

D. Calculation of $4f^15d^1 \rightarrow 4f^2$ emission intensities

Table II, column 4, lists the energies of the 15 $4f^2$ levels derived in the present work from the observation of the $4f^15d^1 \rightarrow 4f^2$ emission spectrum. Table II, column 5, indicates the experimental values of the $4f^15d^1 \rightarrow 4f^2$ emission transition relative intensities from the lowest level Γ_{3u} of the excited configuration. The theoretical values of these intensities were evaluated by a direct calculation and are listed for comparison in column 6.

The lowest (Γ_{1g}) level of $4f^2$ contains about 96.4% $^3H_4$. The composition of the ground Γ_{3u} level of $4f5d$ (in %) is

$$42.9\ ^3F_2 + 38.9\ ^3H_4 + 12.5\ ^3H_5 + 2.9\ ^3G_4 + 0.5\ ^3G_5 + \cdots, \tag{13}$$

so that Γ_{3u} is 98% high spin. Consequently, strong transitions are observed towards the triplet states of the ground configuration whereas the transitions towards the singlet $^1G_4$ and $^1D_2$ multiplets are vanishingly small. In Table II, the value for the first $\Gamma_{3u} \rightarrow \Gamma_{4g}$ emission transition is arbitrarily set to 1.0. The relative intensities of transitions terminating upon $^3H_5$ are calculated rather weaker than observed. Within a given multiplet, however, the relative intensities of the components match fairly well the experimental ratios. For instance, the intensities of lines from $4f5d$ Γ_{3u} towards $4f^2$ $^3H_4$ Γ_5 and Γ_4, are in a ratio of 1.1 (experimental) and 0.7 (calculated). In the same way, the transitions ending on $4f^2$ $^3H_5$ Γ_5 and $a\Gamma_4$ are in the ratios 4.3 (observed) and 3.4 (calculated) while the experimental and calculated values of the transition towards $4f^2$ $^3H_5$ $b\Gamma_4$ are both very small. The transition towards $4f^2$ $^3H_5$ Γ_5 is the strongest in the observed spectrum and is greatly underestimated in the calculated spectrum. Considering the transitions towards the $^3H_6$ multiplet, the relative intensities towards $b\Gamma_5$ and $a\Gamma_5$ are equal to 6.7 (observed) and 5.1 (calculated), respectively, while both the observed and calculated intensities towards Γ_4 are small. Among the allowed transitions towards $^3F_2$, only the one terminating upon Γ_5 is strong.

A variation of the R^k's does not improve the agreement between experimental and calculated intensities. The latter contain a small contribution from $6p$ electrons since the $4f^2$ configuration was analyzed on an enlarged basis $4f^2 + 4f6p$.[8] The radial integral $\langle 5d|r^1|6p\rangle = 1.35$, while $\langle 5d|r^1|4f\rangle = 0.64$, so that the $4f5d \rightarrow 4f6p$ transition intensities are stronger than those of $4f^15d^1 \rightarrow 4f^2$. If $\langle 5d|r^1|6p\rangle$ is set equal to zero, the disagreement between experimental and calculated values is accentuated. Lowering the spin-orbit coupling constant $\zeta(5d)$, without changing the other parameters, does not change significantly the global agreement. However, it modifies drastically the position of the Γ_{1u} level.

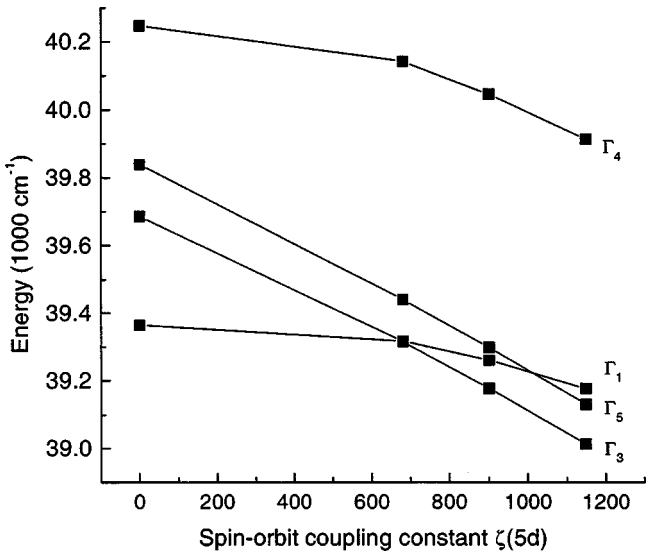

FIG. 10. Variation of the energies of the lower crystal field levels of the $4f^15d^1$ configuration with the spin-orbit coupling constant $\zeta(5d)$.

Thus Γ_{1u} becomes the ground state of the excited configuration for $\zeta(5d) = 680\ cm^{-1}$ and rises 350 cm^{-1} above Γ_{3u} and Γ_{5u} for $\zeta(5d) = 0$. Figure 10 shows the displacement of the four lowest crystal field levels of $4f5d$ when the spin-orbit coupling constant is varied from 0 to 1148 cm^{-1}.

The origin of the transition probabilities can be sought for in the wave vector compositions and in the values of the relevant matrix elements. The J mixing is weak in the ground configuration and is most pronounced in the $^3H_6$ multiplet term, which contains a 6% $^3F_2$ admixture. Table V lists the components of the emitting and terminal levels and the values of the largest matrix elements $\langle M_2|C_p^1|M_1\rangle$. However, these matrix elements do not give the whole story since the meaningful terms are the products $\langle M_2|C_p^1|M_1\rangle \cdot \langle 4f|r^1|5d\rangle \cdot z(M_2,N_2) \cdot z(M_1,N_1)$, which take into account the amounts of M_1 and M_2 components in wave vectors N_1 and N_2, respectively. Therefore, in each cell of Table V, the approximate contribution of that particular term to the total intensity from $\Gamma_{3u} \rightarrow {}^3H_4$, $^3H_5$,... has been indicated. The transitions towards $^3H_4$ and $^3F_2$ are genuine $^3H_4 \rightarrow {}^3H_4$ and $^3F_2 \rightarrow {}^3F_2$ transitions, respectively, given the large amounts of those kets in the emitting and terminal levels. This is not the case for the $\Gamma_{3u} \rightarrow {}^3H_5$ transition, which is calculated about twice too small. Two-thirds of this intensity comes from a $^3G_4 \rightarrow {}^3H_5$ transition, despite the small amount of $^3G_4$ in the initial level, and only 33% comes from $^3H_5 \rightarrow {}^3H_5$. The $^3G_4$ levels lie about 4500 cm^{-1} above Γ_{3u}, so that the admixture is very weak. It is noteworthy that a lowering of $^3G_4$ (which cannot be obtained with the interactions which have been considered) would achieve a more efficient mixing and therefore a significant and selective increase of that particular transition intensity.

E. Configuration interaction

Considering the discrepancies which have been found above in the simulation of the transition intensities, it can be

TABLE V. Relevant matrix elements $\langle M_2|C_p^1|M_1\rangle$ for the electric dipole transitions $\Gamma_{3u}(4f5d)|SLJ)\rangle \rightarrow 4f^2|S'L'J'\rangle$. Only values with modulus >0.15 are listed. Refer to Sec. IV D for the explanation of the contents.

$4f^2$ level $S'L'J'\rightarrow$	$^3H_4$		$^3H_5$		$0.94\ ^3H_6+0.06\ ^3F_2$		$^3F_2$	
$4f5d$ level $SLJ\downarrow$	M_2,M_1	Value	M_2,M_1	Value	M_2,M_1	Value	M_2,M_1	Value
42.9 $^3F_2$							0,1	−0.279
						(33%)	2,1	−0.228
							−2,−2	0.323
								(100%)
38.9 $^3H_4$	−4,−4	−0.232						
	−2,−3	−0.154						
	−2,−1	−0.174						
		(100%)						
12.5 $^3H_5$			−2,−1	−0.175				
			−4,−4	−0.187				
				(33%)				
2.9 $^3G_4$			0,0	0.387				
			0,1	0.300				
			1,2	−0.190				
			−2,−2	0.355				
			−3,−2	−0.410				
			−4,−4	0.232				
			4,5	0.519				
				(66%)				
0.5 $^3G_5$					−2,−2	0.369		
					3,2	0.391		
					4,4	0.292		
					−4,−5	0.484		
						(66%)		

questioned whether some configuration interaction is able to modify the $4f5d$ spectrum in order to improve the simulations. The only acceptable configurations are $4fnl$, with l even. The nearest configurations respecting this condition are $4f6s$ and $4f5g$, the mean energies of which lie theoretically at 84 000 and 205 000 cm^{-1} above that of $4f^2$, respectively. The present experimental results for $PrCl_6^{3-}$ could possibly indicate that the lowest level of $4f6s$ is about 47 000 cm^{-1} above $4f^2$ $[^3H_4]$ Γ_{1g}.

The matrix elements for the two-electron electrostatic interaction between $4f5d$ and $4fnl$ contain the product of $6j$ and $3j$ symbols:

$$\begin{Bmatrix} 3 & l & L \\ 2 & 3 & k \end{Bmatrix} \times \begin{pmatrix} 3 & k & 3 \\ 0 & 0 & 0 \end{pmatrix} \times \begin{pmatrix} 2 & k & l \\ 0 & 0 & 0 \end{pmatrix}. \qquad (14)$$

On the other hand, the expression for the crystal field interaction between $4f5d$ and $4fnl$ contains the term

$$B_q^k(5dnl) \times \begin{pmatrix} 2 & k & l \\ 0 & 0 & 0 \end{pmatrix}. \qquad (15)$$

For the $4f5d/4f6s$ interaction, $l=0$, and conditions (14) and (15) impose $k=2$. Concerning the two-electron interaction, the only interactions occur between ^1F and ^1F terms on the one hand and ^3F and ^3F terms on the other in $4f5d$ and $4f6s$, respectively. The theoretical value for the $R^2(f,d,f,s)$ integral is 2740 cm^{-1}. Since there is no second-order CFP in O_h symmetry, no crystal field interaction exists between the two configurations. The global interaction between $4f5d$ and $4f6s$ therefore seems to be negligible.

Another possible interaction is that between $4f5d$ and $4f5g$. In this case, $l=4$ so that k can be equal to 2, 4, or 6. The electrostatic interaction is allowed between all terms in $4f5d$ and $4f5g$ with the same SL. The theoretical values of the $R^2(f,d,f,g)$ integrals are 2594, 911, and 506 cm^{-1} for $k=2$, 4, and 6, respectively. The configuration interaction utilizing these values produces a negligible effect on $4f5d$. Concerning the crystal field interaction, the theoretical values of the $\langle d|r^k|g\rangle$ radial integrals are equal to 50 and 1350 for $k=4$ and 6, respectively. The latter value is about 70 times the magnitude of $\langle f|r^6|f\rangle$. Since $B_0^6(4f,4f)$ is of the order of 600 cm^{-1}, one can expect $B_0^6(5d5g)$ values in the order of 10^4 cm^{-1} or more. This interaction is likely to drastically perturb the $4f5d$ levels. This track should be explored when more lines of the $4f5d$ configuration have been assigned.

V. CONCLUSIONS

Well-resolved $4f^N$-$4f^{N-1}5d^1$ absorption and emission spectra have been obtained for the lanthanide ion Pr^{3+} in

cubic host lattices. In emission, this has enabled detailed band assignments to be made for the transitions from the lowest $4f^15d^1$ crystal field level, Γ_{3u}, to terminal $4f^2$ crystal field levels. Two vibrational progressions dominate the spectra: that of the totally symmetric $PrCl_6$ stretching mode and that of a totally symmetric $PrCs_8$ lattice mode. The displacement of the $4f^15d^1$ potential energy minimum from that of $4f^2$ is small, however. The ultraviolet absorption and synchrotron excitation spectra have been assigned to two groups of bands involving $4f^2(\Gamma_{1g})\rightarrow(\Gamma_{4u})$ $4f^15d^1$ electronic transitions with extensive vibrational structure. Naturally, the excitation spectra look (and are calculated to be) very different from that recently reported for $LiYF_4:Pr^{3+}$, where three bands of similar intensity appear between 46 400 and 70 000 cm^{-1}. In the present case of $Cs_2NaYCl_6:Pr^{3+}$, strong bands are observed in the lower-energy part of the spectrum (40 000–46 500 cm^{-1}) and weaker ones at the higher-energy part (52 600–71 000 cm^{-1}). The energy gap is expected from the large B_0^4 CFP of the *d* electron. Sharp lines are observed in the window between these groups, and the assignment of these additional features to $4f^2\rightarrow4f^16s^1$ transitions or to ligand-to-metal charge-transfer transition bands requires further, more detailed investigations. The energy levels and eigenvectors of the crystal field levels of the $4f^15d^1$ configuration have been utilized together with those of $4f^2/4f^16p^1$ in order to simulate the intensities in the absorption and emission spectra. The agreement is satisfactory for the latter, but the comparison with experimental data may be premature for the much more limited results from absorption spectroscopy. Finally, we note that caution must be exercised when comparing simulated absorption spectra with excitation spectra since nonradiative pathways to the emitting state also require consideration. It has been remarked[33] that all types of rare-earth sites (for example, clusters of ions) are observed in absorption spectra, whereas a single type of site may be selected in excitation spectra by judicious choice of the emission wavelength. However certain nonradiative pathways from the absorbing state to the emitting state may be blocked and/or efficient energy transfer may occur from an impurity center to the luminescent state.

The large Stokes gap between the emission and absorption spectra has been rationalized by the energy level calculations, since the first allowed emission transition corresponds to $\Gamma_{3u}\rightarrow\Gamma_{4g}$, whereas the first allowed absorption transition is $\Gamma_{1g}\rightarrow\Gamma_{4u}$. The considerable broadening of the emission spectrum with increasing temperature is due to thermal population of Γ_{5u}, with the less restrictive selection rules for electric dipole transitions to all Γ_{2g}, Γ_{3g}, Γ_{4g}, and Γ_{5g} terminal states. The poorly resolved emission spectrum of $Cs_2NaPrCl_6$, compared with that of $Cs_2NaYCl_6:Pr^{3+}$, is attributed at least in part to the removal of degeneracy of the first excited state (as well as of terminal degenerate crystal field levels), with consequent blurring of features.

The most notable of the parameter values employed in the $4f^15d^1$ energy level calculation is the large value of $B_0^4(d)$. Since the crystal field parameter is large, the state eigenvectors are much more extensively mixed than for the f^2 configuration. This mixing of states of f^1d^1 would enable the Judd-Ofelt effective baricentre approximation to become more valid than it would be for "pure" f^1d^1 states. The highest f^1d^1 level is calculated to be Γ_{4u} at 72 650 cm^{-1}. Note that in the noncentrosymmetric system $PrCl_3$ the interconfigurational mixing of $4f^2$ with both $4f^15d^1$ and $4f^16p^1$ is permitted, as well as that of $4f^15d^1$ with $4f^16p^1$,[66] but in the centrosymmetric system $PrCl_6^{3-}$ only $4f^16p^1$ (and not $4f^15d^1$) can mix with $4f^2$.[8] It is interesting that the lowest *SLJ* term of $4f^15d^1$ is of predominantly singlet character in the $PrCl_3$ system,[66] but of high spin in the present case. The extent of mixing of the $4f^15d^1$ configuration with others, such as $4f5g$ and $4f6s$ has been explored in the present study, but detailed answers must await a more complete experimental analysis of the energy level structure of the $4f^15d^1$ configuration.

Dorenbos has recently rationalized the relative $4f^N$-$4f^{N-1}5d^1$ transition energies of over 300 compounds containing Ln^{3+} and stated that the Ce^{3+}-Pr^{3+} energy gap is $12\,240\pm750$ cm^{-1} in 64 of these.[67] In the present case, the accurately determined energy gap between Pr^{3+} and Ce^{3+} in Cs_2NaYCl_6 is 10 821 cm^{-1}, which lies outside this range. This disagreement underlines the fact that the $4f^15d^1$ energy in $Cs_2NaYCl_6:Pr^{3+}$ is the lowest reported so far for Pr^{3+} in halide hosts.

ACKNOWLEDGMENTS

We thank Dr. Jun Lin for technical assistance. Financial support is acknowledged under the Hong Kong City University Grants Commission Research Grant No. CityU 1098/01P.

APPENDIX

The angular part of the matrix elements for the calculation of the electric dipole transitions between configurations (l_1,l_2) and (l_1',l_2') is

$$\langle(l_1,l_2)SLJM_J|C_p^1|(l_1',l_2')S'L'J'M_{J'}\rangle=\{1-[1-(2)^{-1/2}]\delta(l_1,l_2)\}\times\{1-[1-(2)^{-1/2}]\delta(l_1',l_2')\}$$
$$\times(-1)^{S'+L'+2J-M_J+l_2}\delta(S,S')[J,J',L,L']^{1/2}\begin{Bmatrix} J & 1 & J' \\ L' & S & L \end{Bmatrix}$$

$$\times\begin{pmatrix} J & 1 & J' \\ -M_J & p & M_J' \end{pmatrix}\Big[(-1)^{L'}\delta(l_2,l_2')[l_1,l_1']^{1/2}\times\begin{Bmatrix} L & 1 & L' \\ l_1' & l_2 & l_1 \end{Bmatrix}\times\begin{pmatrix} l_1 & 1 & l_1' \\ 0 & 0 & 0 \end{pmatrix}$$

$$+(-1)^{l_1'+l_2'+L}\delta(l_1,l_1')[l_2,l_2']^{1/2}\times\begin{Bmatrix} L & 1 & L' \\ l_2' & l_1 & l_2 \end{Bmatrix}\begin{pmatrix} l_2 & 1 & l_2' \\ 0 & 0 & 0 \end{pmatrix}$$

$$+(-1)^{L+L'+S}\delta(l_1,l_2')[l_2,l_1']^{1/2}\times\begin{Bmatrix} L & 1 & L' \\ l_1' & l_1 & l_2 \end{Bmatrix}\times\begin{pmatrix} l_2 & 1 & l_1' \\ 0 & 0 & 0 \end{pmatrix}$$

$$+(-1)^{l_1'+l_2'+S}\delta(l_2,l_1')[l_1,l_2']^{1/2}\times\begin{Bmatrix} L & 1 & L' \\ l_2' & l_2 & l_1 \end{Bmatrix}\times\begin{pmatrix} l_1 & 1 & l_2' \\ 0 & 0 & 0 \end{pmatrix}\Big]$$

with $[l]=(2l+1)^{1/2}$.

[1] J. P. Morley, T. R. Faulkner, and F. S. Richardson, J. Chem. Phys. **77**, 1710 (1982).
[2] P. A. Tanner, Mol. Phys. **57**, 697 (1986).
[3] T. R. Faulkner and F. S. Richardson, Mol. Phys. **36**, 193 (1978).
[4] J. Sztucki, Chem. Phys. Lett. **203**, 383 (1993).
[5] R. Acevedo, P. A. Tanner, T. Meruane, and V. Poblete, Phys. Rev. B **54**, 3976 (1996).
[6] P. A. Tanner, V. V. R. K. Kumar, C. K. Jayasankar, and M. F. Reid, J. Alloys Compd. **215**, 349 (1994).
[7] A. J. Berry, R. G. Denning, and I. D. Morrison, Chem. Phys. Lett. **266**, 195 (1997).
[8] P. A. Tanner, C. S. K. Mak, and M. D. Faucher, J. Chem. Phys. **114**, 10860 (2001).
[9] A. Furrer, H. U. Güdel, and J. Darriet, J. Less-Common Met. **111**, 223 (1985).
[10] P. A. Tanner, S. Xia, Y.-L. Liu, and Y. Ma, Phys. Rev. B **55**, 12 182 (1997).
[11] A. J. Berry, I. D. Morrison, and R. G. Denning, Mol. Phys. **93**, 1 (1998).
[12] E. Loh, Phys. Rev. **175**, 533 (1968).
[13] E. Loh, Phys. Rev. **158**, 273 (1967).
[14] E. Loh, Phys. Rev. A **140**, A1463 (1965).
[15] W. T. Carnall, P. R. Fields, and R. Sarup, J. Chem. Phys. **51**, 2587 (1969).
[16] M. C. Downer, in *Laser Spectroscopy of Solids II*, edited by W. M. Yen (Springer-Verlag, Berlin, 1989), p. 29.
[17] Y. M. Cheung and S. K. Gayen, Phys. Rev. B **49**, 14 827 (1994).
[18] B. Q. Xie, Y. M. Cheung, and S. K. Gayen, Phys. Rev. B **47**, 5557 (1993).
[19] S. K. Gayen, B. Q. Xie, and Y. M. Cheung, Phys. Rev. B **45**, 20 (1992).
[20] L. van Pieterson, M. F. Reid, R. T. Wegh, and A. Meijerink, J. Lumin. **94**, 79 (2001).
[21] T. Jüstel, J. C. Krupa, and D. U. Wiechert, J. Lumin. **93**, 179 (2001).
[22] R. W. Schwartz and P. N. Schatz, Phys. Rev. B **8**, 3229 (1973).
[23] J. C. van't Spijker, P. Dorenbos, C. W. E. van Eijk, M. S. Wickleder, H. U. Güdel, and P. A. Rodnyi, J. Lumin. **72–74**, 786 (1997).
[24] M. Laroche, M. Bettinelli, S. Girard, and R. Moncorgé, Chem. Phys. Lett. **311**, 167 (1999).
[25] B. F. Aull and H. P. Jenssen, Phys. Rev. B **34**, 6647 (1986).
[26] Th. Pawlik and J.-M. Spaeth, J. Appl. Phys. **82**, 4236 (1997).
[27] K.-H. Park and S.-J. Oh, Phys. Rev. B **48**, 14 833 (1993).
[28] L. J. Nujent, R. D. Baybarz, J. L. Burnett, and J. L. Ryan, J. Phys. Chem. **77**, 1528 (1973).
[29] G. Blasse, Struct. Bonding (Berlin) **26**, 43 (1976).
[30] L. van Pieterson, M. Heeroma, E. de Heer, and A. Meijerink, J. Lumin. **91**, 177 (2000).
[31] A. M. Srivastava and S. J. Duclos, Chem. Phys. Lett. **275**, 453 (1997).
[32] L. van Pieterson, R. T. Wegh, A. Meijerink, and M. F. Reid, J. Chem. Phys. **115**, 9382 (2001).
[33] M. F. Reid, L. van Pieterson, R. T. Wegh, and A. Meijerink, Phys. Rev. B **62**, 14 744 (2000).
[34] P. A. Tanner, C. S. K. Mak, and M. D. Faucher, Chem. Phys. Lett. **343**, 309 (2001).
[35] L. R. Morss, M. Siegal, L. Stenger, and N. Edelstein, Inorg. Chem. **9**, 1771 (1970).
[36] K. S. Aleksandrov, A. F. Bovina, V. N. Voronov, M. V. Gorev, I. M. Iskornev, S. V. Melnikova, S. V. Misjul, F. Prokert, and I. N. Flerov, Jpn. J. Appl. Phys., Suppl. **24**, No. 24-2, 699 (1985).
[37] G. P. Knudsen, F. W. Voss, R. Nevald, and H.-D. Amberger, in *Rare Earths in Modern Science and Technology*, edited by G. J. McCarthy, H. B. Silber, and J. J. Rhyne (Plenum, New York, 1982), Vol. 3, p. 335.
[38] M. Laroche, S. Girard, J. Margerie, R. Moncorgé, M. Bettinelli, and E. Cavalli, J. Phys.: Condens. Matter **13**, 765 (2001).
[39] L. Brewer, J. Opt. Soc. Am. **61**, 1666 (1971).
[40] L. R. Elias, W. S. Heaps, and W. M. Yen, Phys. Rev. B **8**, 4989 (1973).
[41] B. Wybourne, *Spectroscopic Properties of Rare Earths* (Wiley, New York, 1965), Chap. 3.
[42] P. A. Rodnyi, V. B. Mikhailik, G. B. Stryganyuk, A. S. Voloshinovskii, C. W. E. van Eijk, and G. F. Zimmerer, J. Lumin. **86**, 161 (2000).
[43] K. H. Park and S. J. Oh, Phys. Rev. B **48**, 14 833 (1993).
[44] G. Ionova, J. C. Krupa, I. Gérard, and R. Guillaumont, New J. Chem. **19**, 677 (1995).
[45] A. S. Voloshinovskii, V. B. Mikhailik, Y. O. Struk, P. A. Rodnyi, C. W. E. van Eijk, and G. Zimmerer, J. Lumin. **79**, 115 (1998).
[46] A. S. Voloshinovskii, M. S. Mikhailik, V. B. Mikhailik, E. N. Mel'chakov, P. A. Rodnyi, C. W. E. van Eijk, and G. Zimmerer, J. Lumin. **79**, 107 (1998).

[47] P. A. Tanner, Chem. Phys. Lett. **145**, 134 (1988).
[48] A. Lentz, J. Phys. Chem. Solids **35**, 827 (1974).
[49] P. A. Tanner and M. Y. Shen, Spectrochim. Acta, Part A **50**, 997 (1994).
[50] L. Ning, S. Xia, and P. A. Tanner, Vib. Spectrosc. **31**, 51 (2003).
[51] G. Meyer, Prog. Solid State Chem. **14**, 141 (1982).
[52] J. R. Dickinson, S. B. Piepho, J. A. Spencer, and P. N. Schatz, J. Chem. Phys. **56**, 2668 (1972).
[53] W. E. Bron and M. Wagner, Phys. Rev. **139**, A223 (1965).
[54] C. W. F. T. Pistorius, J. Chem. Phys. **29**, 1328 (1958).
[55] C. W. F. T. Pistorius, Bull. Soc. Chim. Belg. **68**, 630 (1959).
[56] B. Henderson and G. F. Imbusch, *Optical Spectroscopy of Inorganic Solids* (Clarendon, Oxford, 1989). p. 208.
[57] H. Yersin, H. Otto, J. I. Zink, and G. Gliemann, J. Am. Chem. Soc. **102**, 951 (1980).
[58] P. N. Schatz, Spectrochim. Acta **21**, 617 (1965).
[59] C. W. Struck and W. H. Fonger, J. Lumin. **10**, 1 (1975).
[60] B. R. Judd, *Operator Techniques in Atomic Spectroscopy* (Princeton University Press, Princeton, 1965), Chap. 4.
[61] R. D. Cowan, *The Theory of Atomic Structure and Spectra* (University of California Press, Berkeley, 1981).
[62] M. D. Faucher and H. J. Kooy, Solid State Commun. **102**, 663 (1997).
[63] W. C. Martin, J. Sugar, and J. L. Tech, Phys. Rev. A **6**, 2022 (1972).
[64] M. F. Reid, L. van Pieterson, and A. Meijerink, J. Alloys Compd. **344**, 240 (2002).
[65] R. D. Cowan, computer program RCN31, Los Alamos National Laboratory, 1981.
[66] D. Garcia and M. Faucher, J. Chem. Phys. **91**, 7461 (1989).
[67] P. Dorenbos, J. Lumin. **87–89**, 970 (2000).